Chapter 7

Modeling molecular line emission from embedded low-mass young stellar objects

Abstract

This chapter presents the results of Monte Carlo models of the molecular excitation and radiative transfer in the envelopes around four young stellar objects. These sources, SMM 1, L1527 IRS, TMC 1, and L1489 IRS, are representative of the full source sample investigated in this thesis. The spherically symmetric inside-out collapse model is found to give a good description of many of the single-dish spectra, and offers constraints on the sound speed a and the age of the sources t. Values for a range between 0.68 km s^{-1} for SMM 1 and 0.17 km s^{-1} for TMC 1; the ages lie between 5.0×10^4 yr for SMM 1 and 3.2×10^5 yr for L1489 IRS. The HCO^+ abundance inferred from the single-dish lines reproduces the line fluxes observed in the interferometer beam to within factors of a few. These differences can easily be explained by deviations from the adopted model on scales of 1000 AU. To derive abundances from interferometer data, it is crucial that a good estimate of any resolved-out large emission is available, or that the discrete (u,v) sampling is explicitly modeled.

Models for the collapse of a cloud core in the presence of rotation or a weak magnetic field are capable of reproducing the observed flattening on a 1000 AU scale observed toward, e.g., L1489 IRS in HCO^+ in the interferometer beam. In the case of a rotating core, the required value to match the observed flattening of the rotation rate, or, equivalently, the centrifugal radius R_c within which all material is collapsed onto a disk, is uncomfortably large, with R_c = 400–800 AU. For a magnetic field strength of 12 μG or more a similar degree of flattening can be produced, but not the observed rotation velocity signature along the major axis. A combination of both mechanisms, and a description of the smooth transition of a collapsing core into a disk, is likely to offer a better model.

To explain the bright HCO^+ and HCN emission which outlines the outflow cavities toward L1527 IRS and SMM 1 in the interferometer beam, a simple model is constructed of a mixing layer between the fast-moving outflow and the molecular envelope. For a mixing layer which extends over one-fifth of the total width of the outflow cavity and maximum flow velocities in the layer of some 20–30 km s^{-1}, the characteristics of the HCO^+ and HCN emission are well reproduced, as are the ^{12}CO 3–2, 4–3, and 6–5 line wings. No enhancements in the molecular abundances are required to match the observed intensities, but an electron fraction of $\sim 10^{-4}$ is needed to explain the molecular excitation. This offers a promising way to

Hogerheijde & van der Tak 1998, in preparation

study the dynamics and chemistry of the interaction of a fast-moving flow and a molecular core.

7.1 Introduction

Molecular line observations using millimeter interferometers and single-dish telescopes provide powerful diagnostics of the envelopes and outflows of embedded low-mass young stellar objects (YSOs). Chapters 2 and 6 (Hogerheijde et al. 1997a, 1998b) show that the integrated single-dish line intensities of HCO^+ and CO agree well with the simple inside-out collapse model of Shu (1977). The interferometer observations of ^{13}CO, $C^{18}O$, and $H^{13}CO^+$ of Chapters 3 and 6 (Hogerheijde et al. 1998a,b) delineate the inner 1000 AU of the envelopes, which may be rotating and flattened, while bright HCO^+ and HCN emission traces the outflow cavities. More detailed modeling of the molecular excitation and line transfer is required to confirm these conclusions, and to better quantify the chemical abundances and their possible variations in the envelopes. In this chapter we construct such models, with special emphasis on the predicted line profiles and the line fluxes in the interferometric beams. We consider first a spherically symmetric model, and then turn to models with cylindrical symmetry including flattening due to rotation and the presence of weak magnetic fields. An important question is how essential these components are to explain the various observations. Another interesting issue is that of the bright HCO^+ and HCN emission associated with the outflow. Can a simple model for a mixing layer between the molecular envelope and the fast-moving outflow explain the prominent emission in these transitions?

The molecular line emission of protostellar envelopes has been modeled to various degrees of complexity. Myers et al. (1996) proposed a straightforward characterization of line profiles from collapsing clouds, which allows parameters like infall velocity to be derived directly, without the need to solve the molecular excitation. Most of the studies which include the solution of the molecular excitation are limited to one-dimensional or spherically symmetric source models. Zhou et al. (1990, 1993), and Zhou (1992) investigated the molecular line emission of the deeply embedded YSO B335 using a spherically symmetric model and a large-velocity gradient method to determine the excitation. Choi et al. (1995) refined this work by using a spherically symmetric Monte Carlo method for the excitation calculations. Hartstein & Liseau (1998) presented model results for H_2O emission of this same source obtained with a spherically symmetric Monte Carlo code specifically designed to handle large optical depths ($\tau \gg 10^4$), while Doty & Neufeld (1997) used a Λ-iteration technique (Rybicki & Hummer 1992) to determine the molecular excitation in dense cloud cores.

For most models with a more complex, axisymmetric or even three-dimensional geometry the molecular excitation has been solved assuming local thermodynamic equilibrium (LTE; e.g., Walker, Narayanan, & Boss 1994; Ohashi et al. 1997b), or using a Sobolev approximation (Zhou 1995). A notable exception is Wiesemeyer (1997), who presented a (computationally intensive) method to solve non-LTE excitation in an axisymmetric source based on Λ-iteration. In this chapter we use a Monte Carlo method to determine the excitation. This method offers an efficient way to obtain the level populations in cases where molecular radiation provides a dominant contribution to the excitation, as is the case for the observed lines of HCO^+ and HCN (Bernes 1979).

The outline of this chapter is as follows. After introducing the essentials of the Monte Carlo code in §7.2, the molecular line emission from cores undergoing spherically symmetric inside-out collapse is investigated in §7.3. Values for the sound speed, the age of the source, and molecular abundances are derived, setting a reference case for the investigation of axisymmetric models in §7.4. In §7.4.1 we consider the collapse of a slowly rotating core (Cassen & Moosman 1981; Terebey, Shu, & Cassen 1984). §7.4.2 investigates the emission from a collapsing, magnetized core as formulated by Galli & Shu (1993a). The effect of an evacuated outflow cavity on the molecular excitation and the emergent line profiles is evaluated in §7.4.3. In §7.5 we turn our attention to the mixing layer set up between the outflow and the molecular envelope, with the specific aim of reproducing the HCO^+ and HCN emission as observed in the OVRO beam. Section 7.6 summarizes our main conclusions.

Throughout the chapter we focus on four sources from our sample: SMM 1, L1527 IRS, TMC 1, and L1489 IRS. These YSOs span the full range in mass ($M_\star \approx 0.2$–$4\ M_\odot$; $M_{\rm env} \approx 0.01$–$8\ M_\odot$), activity ($L_{\rm bol} \approx 0.7$–$77\ L_\odot$), and evolutionary state of our sample. In addition they exhibit various intriguing features of the molecular line emission like flattening, rotation, the association of bright HCO^+ and HCN with the outflow, and possible infall signatures in the line profiles. To derive quantitative information from the interferometer observations in particular, detailed modeling is essential. The aim of this chapter is not to fully explore the parameter space of each of the considered models. Rather, we derive best-fit parameters by eye to the spherically symmetric models in §7.3, and use these as starting points for the subsequent axisymmetric models. The latter serve to illustrate the influence of rotation, magnetic fields, and the presence of an outflow on the various observations.

7.2 The Monte Carlo code

Like all Monte Carlo codes, our approach to solving the excitation and radiation transfer in molecular clouds is ultimately based on the method presented by Bernes (1979). It takes into account excitation due to collisions and radiation in a spherically or axisymmetric source geometry. The source is divided into a number of cells, each with a constant density, kinetic temperature, molecular abundance, electron fraction, turbulent velocity width, and systematic velocity vector. Together, these fully describe the source. The boundaries of the cells can be chosen such that the parameters vary smoothly from cell to cell. For example, in a density distribution which follows a radial power law as predicted by models of protostellar collapse, the cell sizes are chosen to increase exponentially outward. This results in a density contrast of less than a factor 2 between adjacent cells, and a smooth gradient in the excitation. Because a single value is used to represent the radiation field for each transition, the maximum line opacity in each cell should not exceed ~ 1. For the models studied in this chapter, typically 15 cells cover the 8000 AU radius source, with cell sizes ranging from 50 AU to 2000 AU.

With this source model and the molecular collision rates, the code determines the molecular excitation in each grid cell. In principle, the mean radiation field $\bar{J}_\nu$ at any point in the cloud can be calculated exactly by integrating the equation of radiative transfer along all lines-of-sight passing through that point, and averaging over 4π steradians. The molecular excitation can then be solved, and a new estimate of $\bar{J}_\nu$ calculated. This procedure is repeated until the solution converges. In practice, to determine $\bar{J}_\nu$ by integrating over all lines-of-sight is too time consuming for all but the simplest source models. Instead, the integration over 4π steradians is replaced by a large number of randomly chosen directions, giving a Monte Carlo estimate of $\bar{J}_\nu$. In our (and Bernes') code, the line-of-sight integrations are replaced by a large number of test photons, originating at the outer edge of the cloud and traveling inward in random directions. Each photon represents a single line-of-sight integration, but contributes to $\bar{J}_\nu$ in each cell it passes through, increasing the computational efficiency. The initial intensity of the photon field is that of the cosmic microwave background ($T_{\rm eff}$ = 2.735 K), which is important for the excitation of (sub)millimeter lines. In each step a photon propagates from its current position to the boundary of the nearest neighboring cell along its path. When a photon has passed through the complete cloud, a new photon is emitted at the edge. During each step, the value of $\bar{J}_\nu$ in the cell is updated.

After a certain number of these steps, making up one iteration, the equations of statistical equilibrium of the molecular excitation are solved, and a new iteration is started. This procedure is repeated until the solution converges. Because of the statistical nature of the Monte Carlo method, the noise in the obtained solution is inversely proportional to the square root of the number of photon passages contributing to $\bar{J}_\nu$ in each cell and each velocity interval. Therefore, the number of photon steps making up a single iteration is doubled each time to increase the effective number of photon passages, until convergence is reached. The required number of iterations depends on the complexity of the model, and is quite sensitive to the ratio between the size of the smallest grid cell to the total volume, and to that of the smallest turbulent line width to the total velocity extent or passband. To get proper convergence, the smallest element in the model has to be sampled by a sufficiently large number of photons. In practice, the spherically symmetric models presented in §3 require 10–20 minutes of CPU time on a SparcUltra. The two-dimensional models take significantly more time to converge. For the models presented in §§7.4 and 7.5, typical calculations lasted several hours, even after making some compromises in, e.g., the number of energy levels included in the evaluation of the signal-to-noise ratio.

Our Monte Carlo code shares many similarities with those of Bernes (1979), Choi et al. (1995), and Spaans (1996). An important difference between our code and that of Spaans, and those of Bernes and Choi et al. lies in the interpretation of the photon packages. In the latter approach they correspond to a statistical sampling of the real photons present in the source. They originate at random positions through spontaneous emission, and are absorbed and give rise to stimulated emission along their path. The number of absorption and stimulated emission events in each cell then determines the excitation. In our code, analogous to Spaans (1996), the photons represent line-of-sight integrations of the equation of radiative transfer, and therefore originate at infinity, or, equivalently, at the outer edge of the source grid. Along their path, absorption, stimulated emission, and spontaneous emission contribute to the evolution of the intensity. The average radiation field in each cell follows from the intensities of the photons present. Apart from book-keeping details, both approaches are equivalent. Another important difference between our code and the one-dimensional codes of Bernes and Choi et al. is that ours is also capable of handling axisymmetric source geometries.

Our code has been tested extensively against an escape probability code (cf. Jansen 1995), and the codes of Bernes (1979) and Choi et al. (1995). For simple source models, our code is in excellent agreement with the escape probability code over a large range of excitation conditions. Comparison with the codes of Bernes and Choi et al. for more complicated source models also reveals close agreement. Only for models with a steep gradient in level populations and with an important contribution of line radiation to the excitation does our code reach a different solution than that of Choi et al. We attribute this to differences in the exact treatment of the velocity profile in the photon propagation and $\bar{J}_\nu$ determination. In this regime, small differences in the intensity of the radiation field can cause a significant shift in the excitation. Although some of the HCO^+ and HCN 4–3 lines in the following sections fall in this regime, the emergent line profiles, most predominantly their line centers, are affected by less than 30%.

In this same regime, we find a lower excitation from the axisymmetric code compared to the spherically symmetric code, affecting the strength of the HCO^+ and HCN 4–3 lines by $\sim$ 50%, but leaving the line profiles unchanged. We are confident that the spherically symmetric code produces correct answers, and limit, for the time being, the use of the axisymmetric code to the 1–0 lines of these species, which are unaffected, and to comparison of the line profiles of the higher transitions.

With the solution to the molecular excitation, a radiative transfer code calculates the sky brightness at any distance and viewing angle, which can then be convolved with a single-dish beam or sampled at the (u, v) positions of an interferometric data set and cleaned. The latter technique is essential to quantitatively interpret the interferometer data, since it explicitly takes into account the resolving-out of large scale emission by an array. In this chapter we carry out calculations for CO, HCO^+, and HCN, including a variety of their isotopomers. The molecular collision rates were taken from Schinke et al. (1985) and Flower & Launay (1985) for CO, Monteiro & Green (1985) and Green (1975) for HCO^+, and Green & Thaddeus (1974) for HCN.

7.3 Spherically symmetric source models

To set the reference case for models with an axisymmetric source geometry, we investigate in this section the spherically symmetric inside-out collapse model as formulated by Shu (1977). The aim is to constrain model parameters like the sound speed a, age t, and molecular abundances $X_{\rm mol}$; and to ascertain how well the simplest case, a spherically symmetric source model, can explain the single-dish and aperture-synthesis observations. In §7.3.1 the inside-out collapse model is introduced, and values for various model parameters are derived. Best-fit values for the free parameters a, t, and $X_{\rm mol}$ are obtained in §7.3.2 from the observed single-dish lines of $C^{18}O$, HCO^+, $H^{13}CO^+$, and $H^{13}CN$. The corresponding prediction for the full data set, including the OVRO integrated intensities, are then compared to the observations.

7.3.1 The inside-out collapse model

A spherically symmetric, self-similar solution to the collapse of an isothermal cloud core has been derived by Shu (1977). This model is fully characterized by two parameters, the isothermal sound speed, a, and the time after the onset of collapse, t. The initial density configuration is that of a singular isothermal sphere, with $\rho = a^2/2\pi G r^2$. Collapse initiates at the center, and a pressure wave travels outward at the sound speed. Material inside the wave front located at $r = at$ is falling inward, while the exterior material remains stationary. At any time t the density is given by

$$\rho(r) = \sqrt{\frac{m_0 a^3}{2tr^3}}\ \frac{1}{4\pi G}\ \mathcal{S}(x), \tag{7.1}$$

where

$$\mathcal{S}(x) = \sqrt{\frac{2x^3}{m_0}}\ \alpha(x), \tag{7.2}$$

$x = r/at$, $m_0 = 0.975$, and $\alpha(x)$ is tabulated by Shu. The asymptotic behavior of α is $\alpha \rightarrow \sqrt{m_0/2x^3}$ for $x \ll 1$, i.e., $\mathcal{S}(x) \rightarrow 1$, and $\alpha(x) = 2/x^2$ for $x \geq 1$, yielding the expression for a singular isothermal sphere. The radius $x = r/at = 1$ is the current location of the collapse expansion wave, while the velocity field is given by $V_r = a\ v(x)$, where $v(x)$ is again tabulated by Shu. For $x \geq 1$, the material is stationary with $v(x) = 0$, while for $x \rightarrow 0$ the velocity approaches free fall, $v(x) \rightarrow -\sqrt{2m_0/x}$.

In addition, to calculate the molecular excitation, the kinetic temperature structure, the molecular abundances, and any turbulent velocity field also need to be provided. For the turbulent component of the velocity field we assume a constant value of 0.2 km s^{-1} throughout the cloud, consistent with the results of Fuller & Myers (1992) and Myers & Fuller (1992) for low-mass dark cloud cores. The molecular abundances are also assumed to be constant throughout the envelopes, and the ^{12}CO abundance with respect to H_2 is fixed at 10^{-4}. Standard isotopic ratios of [^{12}CO]:[^{13}CO]=65:1, [^{12}CO]:[$C^{18}O$]=500:1, and [^{12}CO]:[$C^{17}O$]=2695:1 are assumed(cf. Wilson & Rood 1994). The abundances of HCO^+ and HCN are derived by fitting the $H^{13}CO^+$ and $H^{13}CN$ observations.

The kinetic temperature is assumed to follow a radial power law of slope -0.4, as is expected for a cloud which is optically thin to the bulk of the heating radiation (cf. Rowan-Robinson 1980). For the envelopes around the Taurus sources this condition is satisfied. In Chapter 6 (Hogerheijde et al. 1998b) it was shown that the temperature exceeds this power law by a factor of a few in the inner few hundred AU of the much more massive envelope around SMM 1. For the sake of simplicity in the model calculations, such a temperature increase is neglected. This approximation does not influence the results for the molecular emission significantly, except for highly optically thick lines like ^{12}CO, and high-temperature tracers such as H_2CO which are not considered here (cf. §6.4.3 of Chapter 6, Hogerheijde et al. 1998b). A kinetic temperature of 28 K at a characteristic radius of 1000 AU is assumed for all four sources. This is close to the value derived in Chapter 6 (Hogerheijde et al. 1998b) for SMM 1, and within a few K of the values predicted by the model calculations of Adams & Shu (1987) for YSOs like those in Taurus. The similarity between the temperatures in the envelope around

Table 7.1. Best-fit results spherically symmetric models

Source	a (km s^{-1})	t (yr)	$X_{\rm mol}$ HCO$^+$	HCN	$\dot{M}^{\rm a}$ ($M_\odot$ yr^{-1})	$M_\star{}^{\rm b}$ ($M_\odot$)	L ($L_\odot$) mod$^{\rm c}$	obs$^{\rm d}$	$M_{\rm env}$ ($M_\odot$) mod$^{\rm e}$	obs$^{\rm f}$
SMM 1	0.68	5.0(4)	6(−9)	3(−8)	7(−5)	3.7	2800	77	4.8	4.3
L1527 IRS	0.23	1.6(5)	8(−9)	...	3(−6)	0.5	14	1.3	0.02	0.03
TMC 1	0.17	2.5(5)	5(−9)	...	1(−6)	0.3	3.2	0.66	0.01	0.01
L1489 IRS	0.23	3.2(5)	9(−9)	...	3(−6)	0.9	27	3.7	0.02	0.02

[a] Mass accretion rate of inside-out collapse model, $\dot{M} = a^3 m_0/G$.
[b] Accreted mass in model $M_\star = \dot{M}t$.
[c] Accretion luminosity in model $L = GM_\star\dot{M}/R_\star$, where $R_\star = 3R_\odot$ is assumed.
[d] Observed bolometric luminosity, from Chapters 2 and 6 (Hogerheijde et al. 1997a, 1998b).
[e] Envelope mass in model, within a $20''$ diameter region.
[f] Dust mass in $19''$ beams, from Chapters 2 and 6 (Hogerheijde et al. 1997a, 1998b).
Note: Notation $a(b) = a \times 10^b$.

SMM 1 and those in the envelopes surrounding the much less luminous Taurus sources is due entirely to the large opacity to the infrared heating radiation in Serpens. For our models we assume an inner radius of 100 AU and an outer radius of 8000 AU. The results do not depend on the exact value of these parameters.

7.3.2 Results

7.3.2.1 Fits to the single-dish data

Best-fit values for the sound speed a, the source age t, and the abundances of HCO$^+$ and HCN were derived from the single-dish line profiles of C^{18}O 2–1 and 3–2, H^{13}CO$^+$ 3–2 and 4–3, and, for SMM 1, H^{13}CN 4–3 and C^{17}O 3–2. The best-fit values are listed in Table 7.1, and the resulting line profiles for the full single-dish data set are presented alongside the observations in Fig. 7.1. The corresponding integrated line intensities are compared to the observed values in Table 7.2. These include intensities of ^{13}CO, C^{18}O, HCO$^+$, H^{13}CO$^+$, HCN, and H^{13}CN 1–0 obtained after sampling the models at the (u, v) positions of the OVRO observations, and cleaning. Since the models do not contain an outflow, directly associated emission features like broad ^{12}CO line wings and bright HCO$^+$ and HCN in the OVRO beam are not reproduced.

The models have been fit by eye, and the derived values are representative values only. However, the intensity and the line profile shape together accurately constrain the sound speed a and age t. The sound speed a determines the mass of the cloud core, and hence the integrated intensity of the optically thin lines. The width of the lines depends on the age t, since the infall velocities increase over time. The wide lines of H^{13}CO$^+$ 4–3 and ^{13}CO 6–5 compared to C^{18}O 2–1 are the results of the larger infall velocities at small radii, since these lines exclusively sample the warm and dense material in this region. The sensitivity of the line intensity and profile shape to a and t give an estimated uncertainty in the derived values of $\sim$ 50% in the age, and approximately 10%–20% in the sound speed, within the framework of the adopted model.

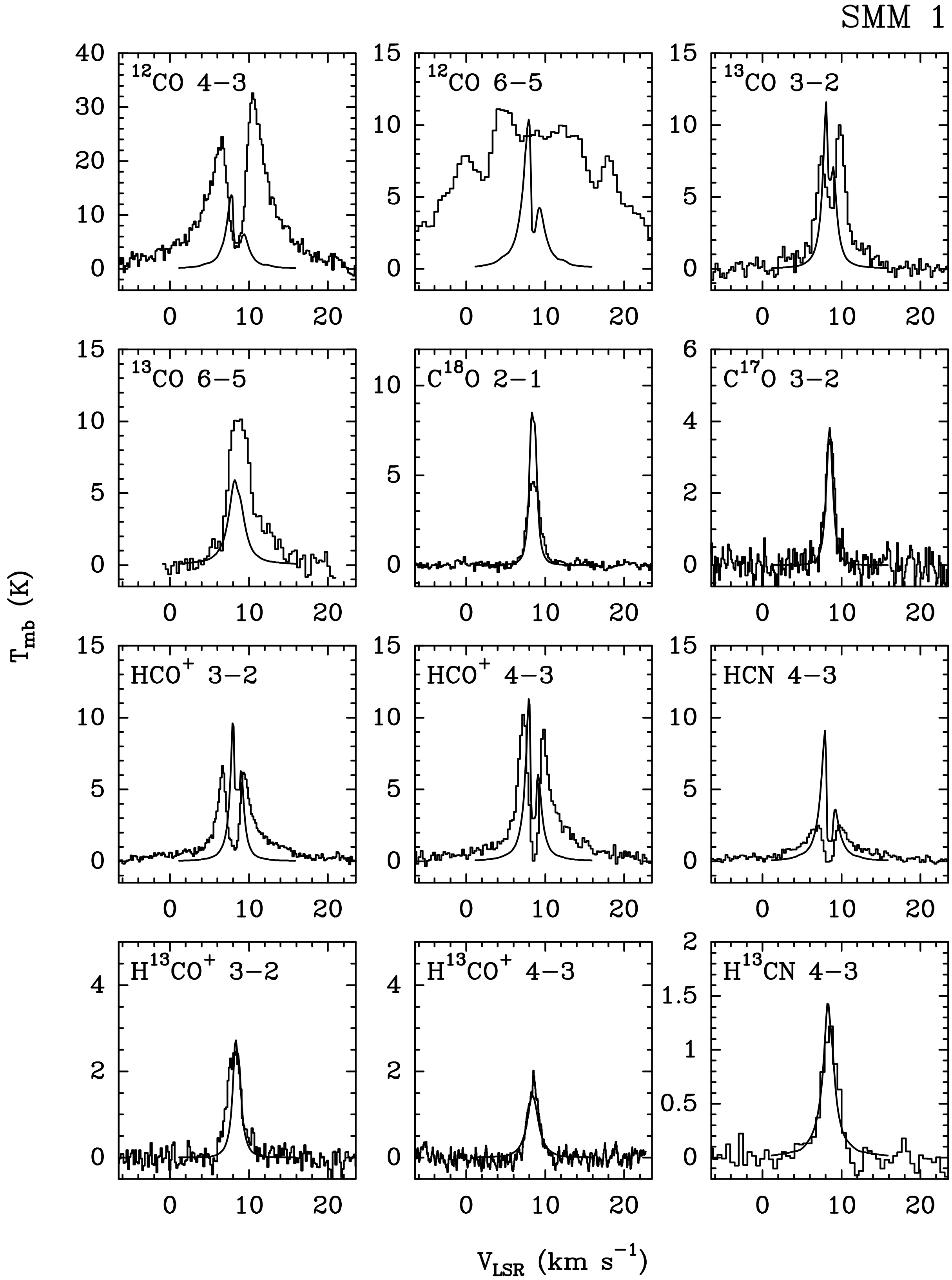

Fig. 7.1 (a) *Spherically symmetric model results superposed on observed single-dish spectra: SMM 1.*

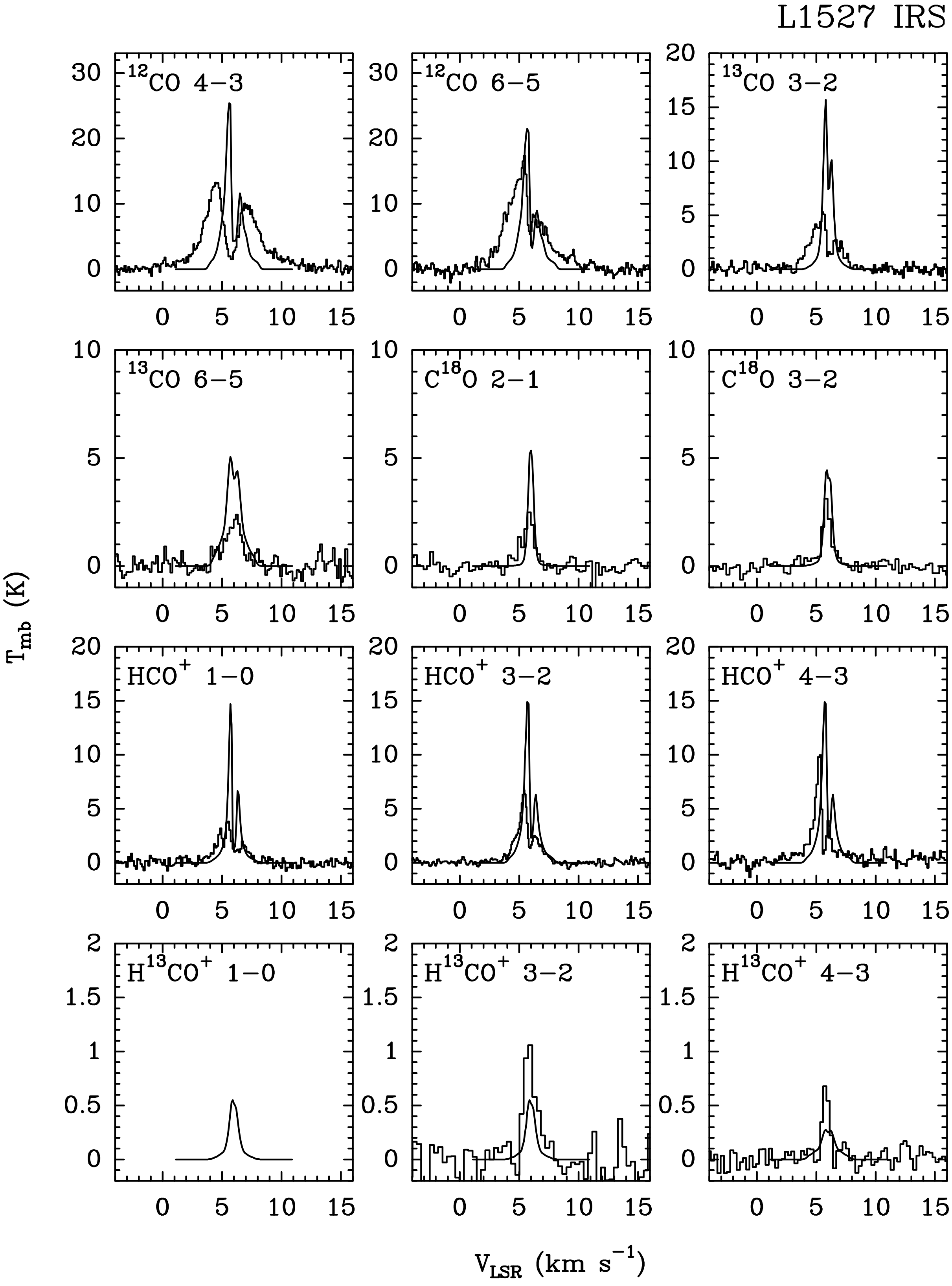

Fig. 7.1 (b) *Model results superposed on observations: L1527 IRS.*

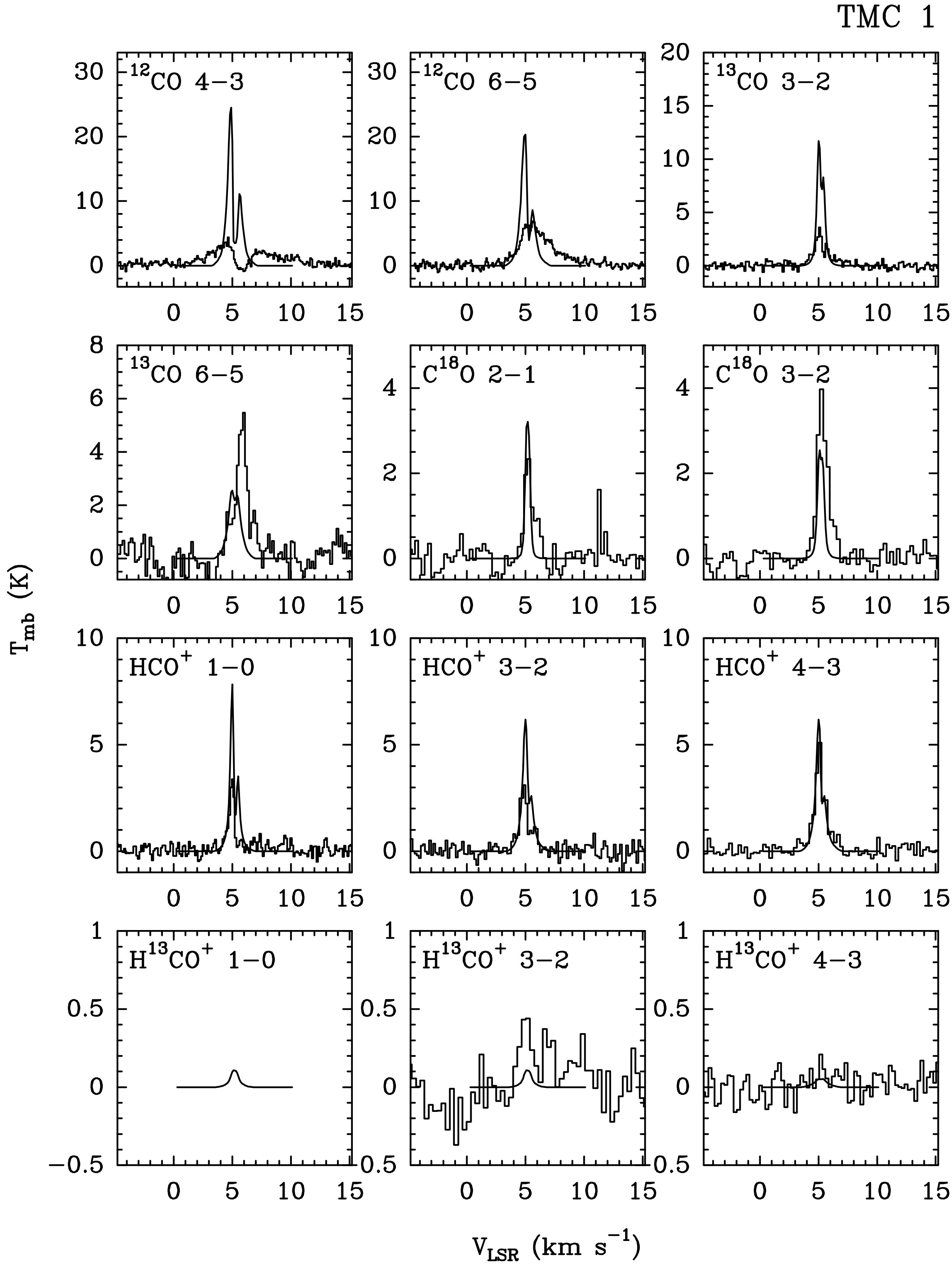

Fig. 7.1 (c) *Model results superposed on observations: TMC 1.*

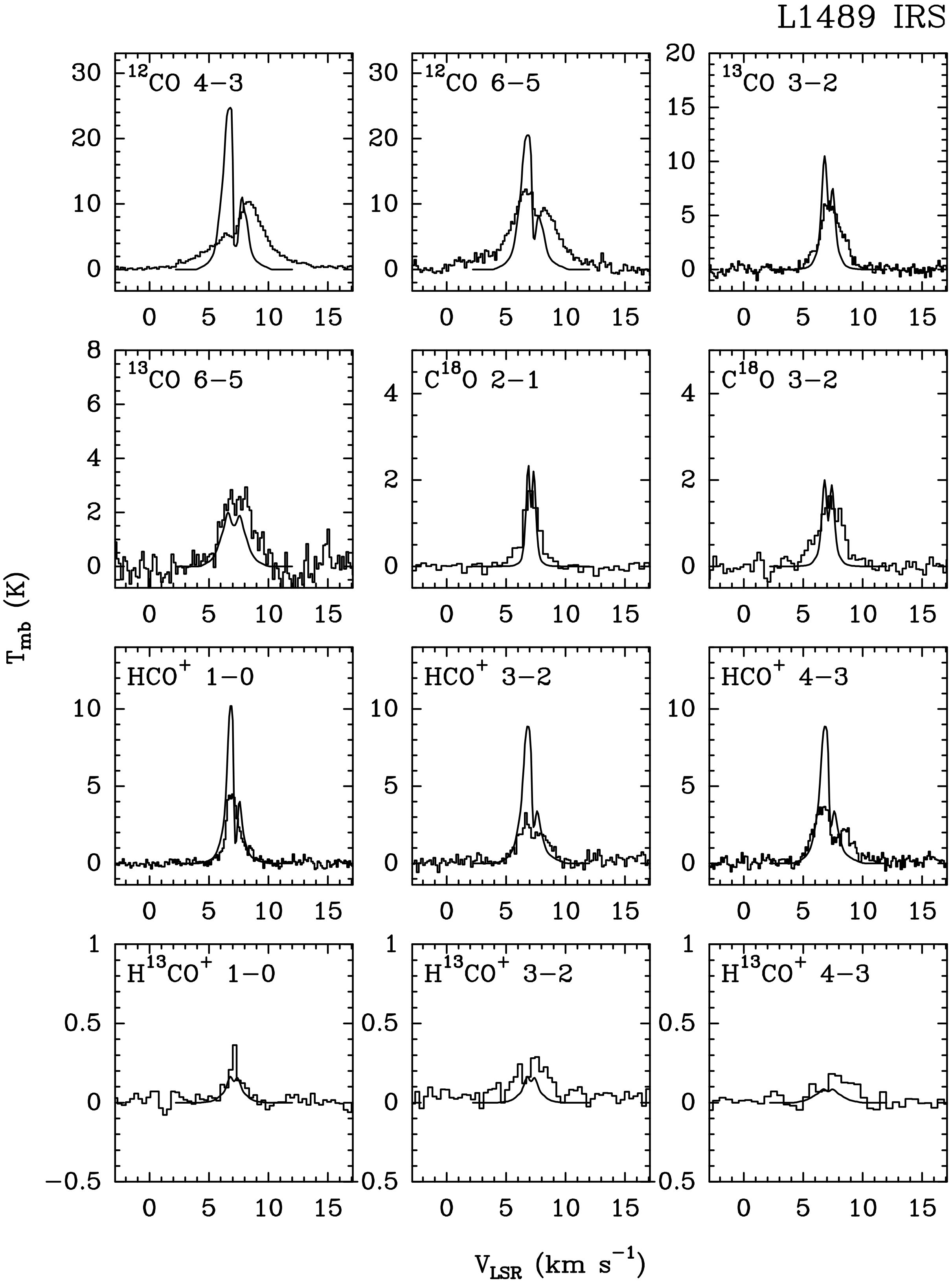

Fig. 7.1 (d) *Model results superposed on observations: L1489 IRS.*

Table 7.2. Comparison of spherically symmetric models and observations

		SMM 1		L1527 IRS		TMC 1		L1489 IRS	
Line	Instrument	obs[a]	mod[b]	obs	mod	obs	mod	obs	mod
^{12}CO 3–2	JCMT	…	27	24	33	21	25	25	44
^{12}CO 4–3	JCMT	232	34	51	43	16	31	45	56
^{12}CO 6–5	CSO	222	25	51	38	21	28	37	49
^{13}CO 1–0	OVRO	2.5	12	1.1	2.7	0.4	1.4	3.6	3.1
^{13}CO 2–1	JCMT	27	17	…	15	…	10	…	15
^{13}CO 3–2	JCMT	36	21	11	20	4.1	12	14	18
^{13}CO 6–5	CSO	41	17	4.1	12	7.1	4.9	8.2	6.9
C^{18}O 1–0	OVRO	1.4	5.6	< 0.5	0.4	0.1	0.2	0.3	0.5
C^{18}O 2–1	JCMT	9.5	11	3.0	4.8	2.3	2.5	3.0	3.1
C^{18}O 3–2	JCMT	…	14	2.8	5.6	4.4	2.7	4.0	3.5
C^{18}O 6–5	CSO	…	3.9	…	1.8	…	0.69	…	0.95
C^{17}O 3–2	JCMT	5.7	4.7	…	1.2	…	0.54	…	0.69
HCO$^+$ 1–0	OVRO	14	16	2.3	11	1.4	5.9	5.5	13
HCO$^+$ 1–0	IRAM	…	13	6.5	11	2.2	5.2	6.7	11
HCO$^+$ 3–2	JCMT	33	17	8.9	15	3.2	7.1	6.9	16
HCO$^+$ 4–3	JCMT	48	20	13	20	5.5	7.3	10.0	18
H^{13}CO$^+$ 1–0	OVRO	1.6	4.2	…	1.0	…	0.4	…	0.8
H^{13}CO$^+$ 1–0	IRAM	…	3.4	…	1.3	…	0.32	0.25	0.73
H^{13}CO$^+$ 3–2	JCMT	5.8	4.1	1.2	0.87	< 0.3	0.16	0.67	0.43
H^{13}CO$^+$ 4–3	JCMT	3.1	3.2	0.35	0.68	< 0.1	0.11	0.61	0.32
HCN 1–0	OVRO	5.0	20	…	12	…	7.2	…	14
HCN 1–0	IRAM	…	21	…	10	…	5.0	…	10
HCN 3–2	JCMT	…	14	…	11	…	5.8	…	12
HCN 4–3	JCMT	18	17	…	15	…	6.6	…	14
H^{13}CN 1–0	OVRO	0.4	4.9	…	1.4	…	0.6	…	1.1
H^{13}CN 1–0	IRAM	…	4.3	…	1.2	…	0.42	…	0.77
H^{13}CN 3–2	JCMT	…	4.3	…	0.65	…	0.16	…	0.35
H^{13}CN 4–3	JCMT	3.0	3.5	…	0.40	…	0.078	…	0.19

[a] Observed integrated intensity in K km s^{-1}.

[b] Integrated intensity of spherically symmetric model, in K km s^{-1}, in beam sizes of the indicated instrument. The interferometer results refer to averages over a $20'' \times 20''$ region.

The derived values of a and t correspond well to previously derived values for L1527 IRS and similar sources (Zhou 1995; Zhou, Evans, & Wang 1996; Naranayan, Walker, & Buckley 1997), and compare favorably with the estimated duration of the class 0 and I stages of a few times 10^4 and a few times 10^5 yr, respectively. The inside-out collapse model predicts a mass infall rate of $\dot{M} = a^3 m_0/G$, which corresponds to 1×10^{-6} $M_\odot$ yr^{-1} to 7×10^{-5} $M_\odot$ yr^{-1} for the inferred values of a. The accreted mass, $\dot{M}t$, then follows as 3.7 $M_\odot$ for SMM 1, 0.46 $M_\odot$ for L1527 IRS, 0.28 $M_\odot$ for TMC 1, and 0.92 $M_\odot$ for L1489 IRS. Assuming a stellar radius of 3 $R_\odot$, the corresponding accretion luminosities exceed the observed bolometric luminosities by factors of 5–35. This is a well known problem (cf. Kenyon et al. 1994), and suggests that most mass accretes onto a circumstellar disk before flowing toward the star at a much lower rate. The envelope masses corresponding to the inferred values of a and t correspond well to the values derived from dust continuum measurements in a 19″ beam (Chapters 2 and 6, Hogerheijde et al. 1997a, 1998b).

In terms of excitation conditions, CO and its isotopes are close to LTE throughout the envelope because the density exceeds the critical density of the observed lines nearly everywhere. Only the excitation of the 6–5 lines falls slightly below LTE in the outer, coldest regions of the envelope, since these levels require temperatures of 40–80 K to be efficiently populated. When modeling CO line emission from YSO envelopes LTE excitation may therefore be safely assumed, except perhaps for the details of self-absorption features in the line centers of ^{12}CO 4–3 and 6–5. The excitation of HCO$^+$ and HCN, for which the observed transitions have critical densities in the range of 10^5–10^7 cm^{-3}, differs significantly from LTE. Only for SMM 1, where the density is largest, are the HCO$^+$ and HCN populations driven close to LTE by their own radiation fields. This illustrates that for such transitions a detailed non-LTE calculation is necessary to obtain accurate results. The increased effort is made worthwhile by the higher sensitivity of these transitions to the density structure of the envelopes.

With a number of exceptions, the single-dish integrated intensities and line profiles are well reproduced by the models (Table 7.2 and Fig. 7.1). Since no outflows are included, their significant contribution to the ^{12}CO line wings is missing (cf. §7.5). The line wings in the spectra of HCO$^+$ and HCN are well fitted by the models, indicating that they are predominantly infall wings rather than outflow wings. Toward SMM 1 the HCO$^+$ and HCN line wings can be fitted by infall, if a sound speed of $a \approx 0.96$ km s^{-1} is adopted.

Other discrepancies in the optically thick lines of ^{12}CO and HCO$^+$ can be seen close to line center. The models of TMC 1 and L1489 IRS produce excess ^{12}CO 6–5 emission, suggesting that the amount and distribution of 50–100 K material around these models is different from that assumed by the model. Excess emission in the lower lines of ^{12}CO and in HCO$^+$ 1–0 can be accounted for by the unrealistic treatment of the outer edge of the envelope in our model, where the density drops to zero outside 8000 AU. In reality, the envelope will merge into the surrounding cloud. A simple analysis shows that in the case of L1527 IRS a column of $N_{\rm H_2} \approx 3 \times 10^{21}$ cm^{-2} at density of $\sim 5 \times 10^4$ cm^{-3} and a temperature of 6 K can absorb all of the excess emission from ^{12}CO 3–2, 4–3, ^{13}CO 3–2, and HCO$^+$ 1–0, without affecting any of the other lines (see Fig. 7.2). Such a column is typical of the diffuse envelope of molecular clouds. The low kinetic temperature of 6 K is derived from the deep self-absorption features in the ^{12}CO 3–2 and 4–3 lines. These discrepancies indicate that the ^{12}CO lines, as well as HCO$^+$ 1–0, are less well suited to trace the envelopes because their intensity and line profile shapes depend sensitively on the surrounding material.

Asymmetries in the profiles of self-absorbed lines, with the blue peak strongest, are often used as indicators of ongoing infall (cf. Mardones et al. 1997; Gregersen et al. 1997). Whereas the model produces this asymmetry in all optically thick lines, the observed spectra reveal it only selectively. This is, again, a result of the large sensitivity of some lines to surrounding material. HCO$^+$ 3–2 and 4–3, which were found to exclusively

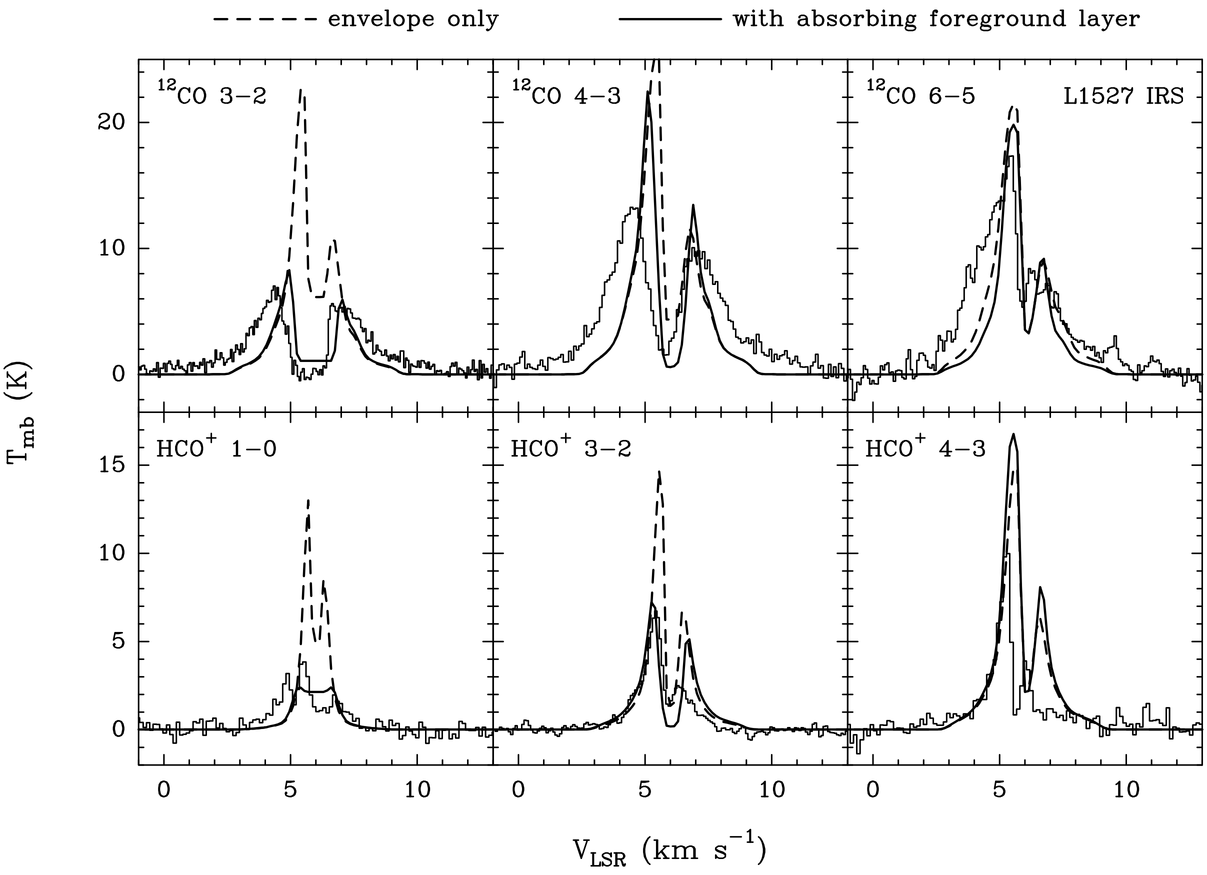

Fig. 7.2. *Model spectra with (solid line) and without (dashed line) an absorbing foreground layer, superposed on the observed spectra toward L1527 IRS. The parameters of the foreground layer are* $n_{\mathrm{H}_2} = 5 \times 10^4$ *cm*$^{-3}$, T_{kin} *=6 K,* ΔV *=0.8 km s*$^{-1}$*, and* $N_{\mathrm{H}_2} = 3 \times 10^{21}$ *cm*$^{-2}$.

trace the envelopes, show the blue asymmetry toward all four sources considered here, and, in fact, toward all sources studied in this thesis whenever self-absorption is present (see Figs. 2.3 and 6.6). This underlines that the presence of infall asymmetry in a self-absorbed line profile should only be interpreted as an indication of continuing infall in lines which exclusively sample the envelope, while its absence cannot be taken as proof that infall has ceased.

Chapter 6 (Hogerheijde et al. 1998b) found that CO may be depleted by a factor of 5 throughout much of the envelope around SMM 1. Further support for depletion is offered by the $C^{18}O$ 2–1 and $C^{17}O$ 3–2 line profiles of Fig. 7.1. The 3–2 profile, which samples gas of $\sim$ 30 K, is well fit by the model, while the 2–1 line at $\sim$ 16 K is overestimated by almost a factor of two. With CO significantly depleted for temperatures below 20 K, the 2–1 line may be brought in closer agreement with the observations. In the $C^{18}O$ 2–1 and 3–2 lines a similar hint of depletion may be seen toward L1527 IRS, another deeply embedded YSO. For the more evolved sources L1489 IRS and TMC 1, the 2–1/3–2 line ratio is well reproduced without depletion.

Table 7.3. Different methods to derive abundances from interferometer data

Source	Input[a]	Method 1[b]	Method 2[c]	Method 3[d]
SMM 1	6.0(−9)	1.0(−8)	1.2(−8)	1.0(−8)
L1527 IRS	8.0(−9)	1.1(−8)	4.1(−8)	1.6(−8)
TMC 1	5.0(−9)	6.5(−9)	2.6(−8)	1.4(−8)
L1489 IRS	9.0(−9)	1.2(−8)	2.5(−8)	2.3(−8)

[a] Input HCO^+ abundance to the model calculations; best-fit values from Table 7.1.

[b] Derived value assuming LTE excitation at the same excitation temperature of both species, and including all spatial scales.

[c] Assuming LTE, and sampling the $H^{13}CO^+$ and $C^{18}O$ results on the discrete (u,v) positions of the respective data sets.

[d] Assuming LTE, and sampling the $H^{13}CO^+$ and $C^{18}O$ results on (u,v) positions within the range of projected baseline lengths common to both data sets.

Note: Notation $a(b) = a \times 10^b$.

7.3.2.2 Fits to the interferometer data

An important question is whether the molecular abundances are constant throughout the envelopes, or whether they are significantly different on the size scales sampled by the interferometer. Using the abundances derived from single-dish lines as described above, integrated intensities in the interferometer beam are obtained by sampling the model results at the (u, v) positions of the OVRO data, and cleaning. With the exception of ^{13}CO, HCN, and $H^{13}CN$ 1–0 toward SMM 1, which suffers from large levels of resolved-out flux, all model intensities agree to within a factor of a few with the observations as seen in Table 7.2. Details like flattening (L1489 IRS, TMC 1), and bright outflow walls (SMM 1, L1527 IRS) are not reproduced by the model (cf. §§7.4 and 7.5). This suggests that the abundance of HCO^+ is not significantly different on these scales, especially since the exact details of the source geometry, and density and temperature distribution are likely to show deviations from the adopted model on these scales. The $H^{13}CN$ 1–0 intensity toward SMM 1 is overestimated by an order of magnitude by the model, suggesting that on small scales the HCN abundance may lower by this same factor compared to the value listed in Table 7.1.

A related question is whether molecular abundances can be directly inferred from the integrated intensity images of interferometer data, or whether detailed model calculations such as carried out above are required. To this end Table 7.3 compares the HCO^+ abundances used in the model calculations with derived values from the model results using three different methods. In all cases the $C^{18}O$ and $H^{13}CO^+$ lines are used, and converted to an HCO^+ abundance with respect to H_2, to minimize optical depth effects. The first method assumes LTE level populations for both species at the same excitation temperature, and uses the unconvolved model intensity distributions. The assumption of LTE in itself overestimates the HCO^+ abundance by 30%–40%, because $H^{13}CO^+$ is more subthermally excited than $C^{18}O$. The $C^{18}O$ opacity of ~ 1 in the envelope of SMM 1 increases the HCO^+ abundance to 1.7 times the model input value.

Much larger differences between the input abundances and the derived values are found after sampling at the (u,v) positions of the OVRO data sets, as done for methods 2 and 3. Both methods use LTE excitation like method 1, and the derived abundances are therefore best compared to the results of method 1. Method 2 samples the model results at the (u,v) positions of the OVRO data sets at 3.4 mm for $H^{13}CO^+$ and 2.7 mm for $C^{18}O$. This overestimates the HCO^+ abundance by a factor of 4 compared to the results of method 1. This difference is due entirely to the variation in levels of recovered flux in $C^{18}O$ and $H^{13}CO^+$, of $\sim 15\%$ and 50%–70% respectively. To a large extent this is caused by the difference in shortest baseline length in units of wavelength at 2.7 and 3.4 mm. Although the same antenna configurations were used for the observations, the shortest baseline in the $C^{18}O$ data is 5–7 kλ, compared to 3–4 kλ for $H^{13}CO^+$.

The third method tries to circumvent this problem by using only those (u,v) positions on projected baseline separations shared by the two data sets. This reduces the difference in derived abundance compared with the values from method 1 to a factor of 2, but does not totally eliminate it. This is explained by the different density regimes traced by $H^{13}CO^+$ and $C^{18}O$ 1–0, and the resulting different sky brightness distributions. Even when these are sampled at the same (u, v) positions, different flux levels are recovered. Only for SMM 1, which has the largest densities of the four sources and therefore an $H^{13}CO^+$ brightness distribution which resembles that of $C^{18}O$, are similar fractions of recovered flux obtained.

As a consequence, to obtain accurate estimates of the molecular abundances on small scales sampled by interferometer data, it is imperative that either a measure of the zero-spacing flux is available, or that detailed model calculations are used which take into account the resolving-out of large fractions of the flux. The latter option is preferable, since it also realistically treats the excitation and opacity.

The results presented in this section show that the spherically symmetric, inside-out collapse model gives a very good description of the envelope structure as traced by single-dish observations. These models also reproduce the integrated flux in interferometers beams, but not the morphology of the emission. In the next sections we elaborate on these models, trying to explain the flattening and possible rotation observed in the aperture synthesis images of some of our sources (§7.4), and the bright HCO^+ and HCN emission outlining the outflows (§7.5).

7.4 Axisymmetric source models

In this section we investigate the effects of the inclusion of an axisymmetric geometry on the molecular emission from a protostellar envelope. §7.4.1 investigates the model of a collapsing, slowly rotating core as developed by Cassen & Moosman (1981) and Terebey et al. (1984). Specifically, we address the question whether this model can explain the flattened, rotating structure seen in the OVRO beam toward some of our sources. §7.4.2 considers the collapse of a weakly magnetized cloud core as formulated by Galli & Shu (1993a) as an alternative explanation for the flattened source structure. For both models L1489 IRS is adopted as an example, and the different density distributions are shown

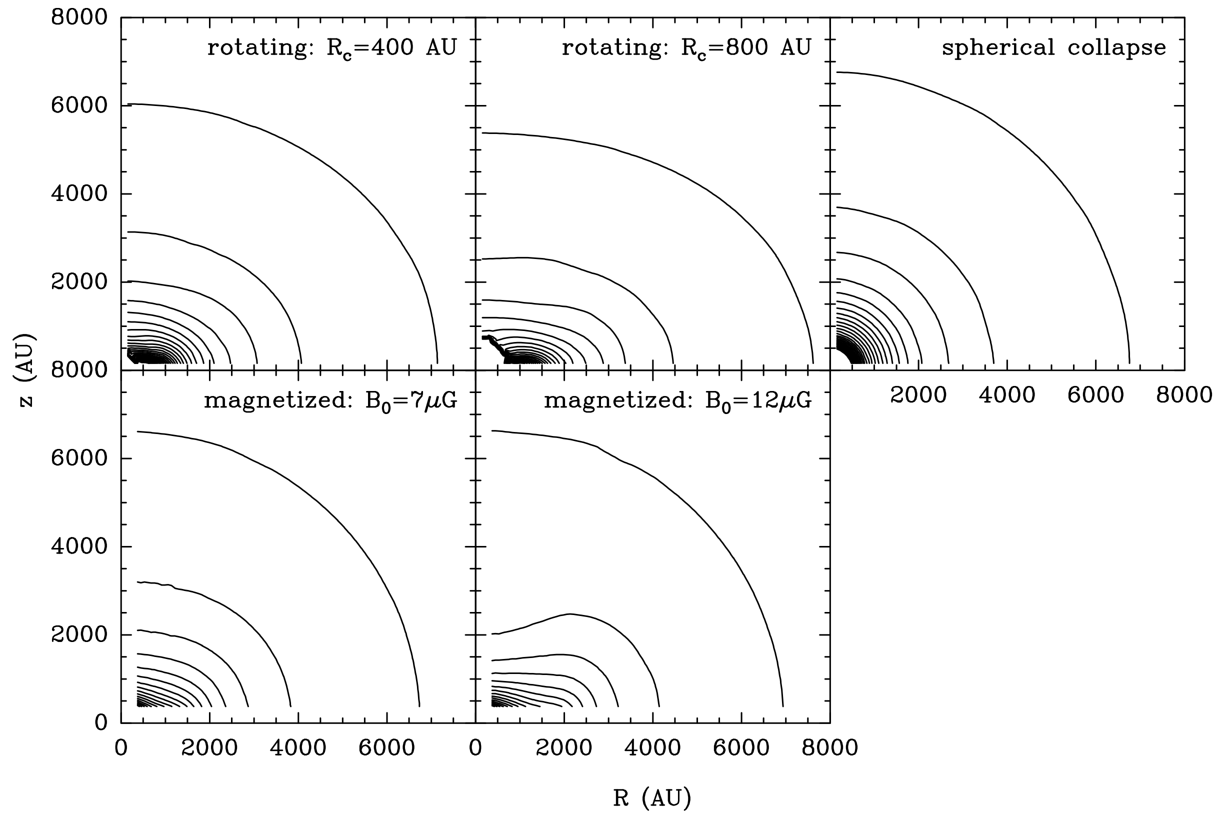

Fig. 7.3. *Comparison of the density distribution of the spherically symmetric model of Shu (1977) (upper right), a slowly rotating collapsing core for two different rotation rates (top left two panels), and a magnetized collapsing core for two different field strengths (bottom two panels). Sound speed a and age t are those of L1489 IRS (Table 7.1). Contours are drawn at intervals of* $n_{\rm H_2} = 1.5 \times 10^4$ *cm*$^{-3}$.

in Fig. 7.3. §7.4.3 examines the effect that an evacuated outflow cavity has on the molecular excitation and the emergent line profiles, taking L1527 IRS as an example.

7.4.1 A slowly rotating, collapsing core

Based on the self-similar collapse model of Shu (1977), Cassen & Moosman (1981) and Terebey et al. (1984) developed solutions for the collapse of a slowly rotating core. In the limit that the rotation period Ω^{-1} is much longer than the time scale for collapse, rotation can be treated as a perturbation to the spherically symmetric model. The density and velocity structure is then given by (see also Adams, Lada, & Shu 1987)

$$\rho(r,\theta) = \sqrt{\frac{m_0 a^3}{2tr^3}}\ \frac{1}{4\pi G}\ \mathcal{R}(u,\theta)\ \mathcal{S}(x), \tag{7.3}$$

where the angle θ is the polar angle, and $\mathcal{S}(x)$ is the solution of the spherical collapse defined in equation (7.2). The dimensionless parameters u and x are defined as $u = r/R_c$ and $x = r/at$, with $R_c = am_0^3t^3\Omega^2/16$ the centrifugal radius. Rotation balances gravity within this radius, and material can only continue to travel inwards through the action of viscosity, e.g., in an accretion disk.

The distorting effects of rotation, which deflects fluid motions toward the equatorial plane, are represented by the function $\mathcal{R}$,

$$\mathcal{R}(u,\theta) = \sqrt{\frac{2\mu_0}{\mu_0+\mu}} \left(1 + \frac{2}{u} P_2(\mu_0)\right)^{-1}, \tag{7.4}$$

where $P_2(\mu_0) = \frac{1}{2}(3\mu_0^2 - 1)$ is the second-order Legendre polynomial, $\mu = \cos\theta$ and $\mu_0 = \cos\theta_0$, with θ_0 the polar angle at position (r,θ) of an originally radial fluid trajectory. μ_0 is given by

$$\frac{\mu_0(1-{\mu_0}^2)}{\mu_0 - \mu} - u = 0. \tag{7.5}$$

For large radii the fluid trajectories are radial, that is $\mu_0 \to \mu$ for $u \to \infty$. Close to the centrifugal radius the trajectories are focussed toward the mid-plane, and $\mu_0 \to \mu^{1/3}$ as $u \to 1$. Formally this leads to a pile-up of material at $r = R_c$, and viscosity is required to transport matter further inward. We assume that for $r \leq R_c$ all material is collapsed onto an accretion disk, which is not included in the model calculations.

Along similar lines, the velocity field is given by

$$V_r = -\frac{av(x)}{\sqrt{2}} \sqrt{1 + \frac{\mu}{\mu_0}}, \tag{7.6}$$

$$V_\theta = \frac{av(x)}{\sqrt{2}} \frac{\mu_0 - \mu}{\sin\theta} \sqrt{1 + \frac{\mu}{\mu_0}}, \tag{7.7}$$

and

$$V_\phi = \frac{av(x)}{\sqrt{2}} \frac{\sin\theta_0}{\sin\theta} \sqrt{1 - \frac{\mu}{\mu_0}}, \tag{7.8}$$

where $v(x)$ is tabulated by Shu (1977).

For the free parameters a and t, as well as for the turbulent velocity width and the temperature distribution, we use the same values as those derived in §7.3.2 for L1489 IRS (see Table 7.1). The deviations due to rotation on the density structure are only significant, i.e. $\mathcal{R} \neq 1$, close to the centrifugal radius R_c. Our aim is to model the observed flattening on a 400–800 AU scale, corresponding to $\Omega = 6.3$–8.3×10^{-14} s^{-1} or 1.9–2.6 km s^{-1} pc^{-1}. Goodman et al. (1993) give a much smaller value of 0.6 ± 0.3 km s^{-1} pc^{-1} for this core based on NH_3 observations on scales of arcminutes, along a position angle which differs by $\sim 35°$ from that inferred in Chapter 3 (Hogerheijde et al. 1998a). The rotation of the core may, however, deviate from that of a solid body, with a larger rotation rate at small radii. Such a configuration is found toward IRAS 16293−2422 by Zhou (1995), where on scales of $\sim$ 8000 AU a value of 6.7 km s^{-1} pc^{-1} is found, compared to 1.1 km s^{-1} pc^{-1} on larger scales.

Figure 7.4 shows the model results for $R_c = 800$ AU of HCO^+ 1–0 compared with the OVRO data of L1489 IRS. The degree of flattening is small even for this large value

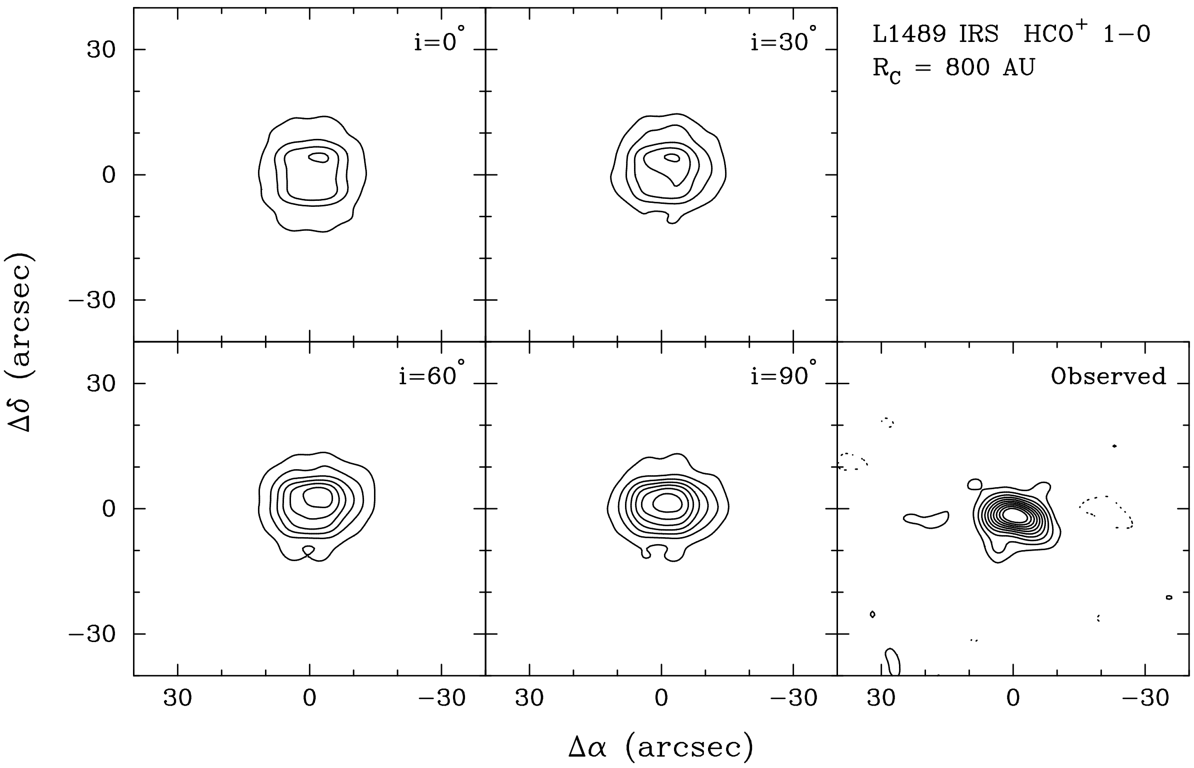

Fig. 7.4. *HCO^+ 1–0 images of a slowly rotating, collapsing core sampled at same (u, v) as OVRO data, and cleaned. Model calculations are for the derived parameters of L1489 IRS (Table 7.1), and include a rotation radius of 800 AU. The observed map is also shown; the position angle of the source equatorial plane is $\sim 65°$. All maps are plotted at the same intensity levels of 0.06 Jy beam^{-1}. An inclination of $i = 0°$ corresponds to a pole-on configuration.*

of R_c, as is the effect of inclination. At these, and higher, rotation rates, the inclusion of a model for the accretion disk, smoothly joined to the collapse solution, becomes important (cf. Cassen & Moosman 1981; Stahler et al. 1994; Koerner & Sargent 1995).

Figure 7.5 shows for various inclinations the synthesized position-velocity diagram of HCO^+ 1–0 for $R_c = 800$ AU, overlaid on the observations of L1489 IRS. In Chapter 3 (Hogerheijde et al. 1998a) the inclination of L1489 IRS is estimated at $\sim 60°$. The figure indicates that this gives reasonable agreement between the model and the observations. The intensity of the model emission is approximately twice that of the observations, which is very reasonable since we do not accurately know the temperature structure, turbulent line width, or HCO^+ abundance on these scales. The extent of the emission along the equatorial direction and in velocity also agrees well with the observations. Additional emission at ± 2 km s^{-1} could originate from the base of the outflow. The model emission also shows small amounts of red- and blueshifted emission at positive and negative offset, respectively. This is due to infalling material in the rotating core (cf. Ohashi et al. 1997b). The weakness of this emission in the observations indicates that infall may have largely ceased in the core. The 1 km s^{-1} wide separation between the model emission peaks is due to absorption by surrounding envelope material which

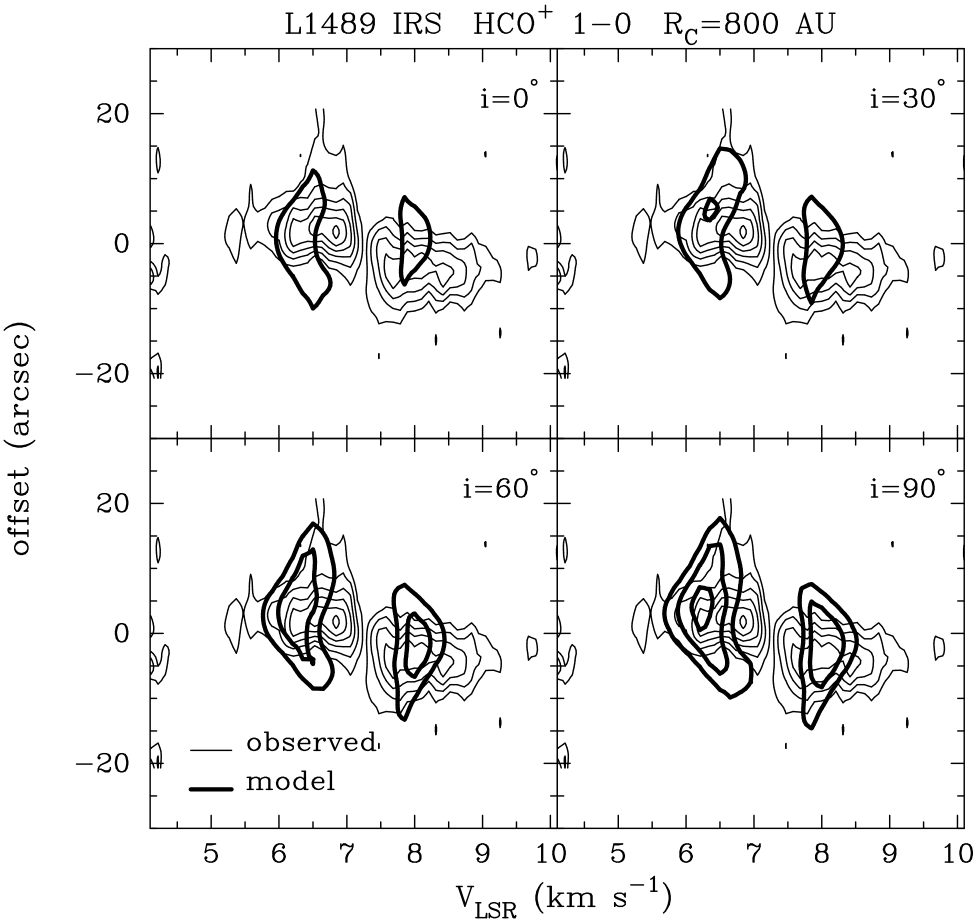

Fig. 7.5 *Overlay of observed position–velocity diagram of HCO^+ 1–0 in the OVRO beam toward L1489 IRS (thin lines), and model results for different inclinations and a rotation radius of 800 AU (heavy lines). For clarity, the model results are plotted at twice the contour intervals of the data, which is 0.35 Jy beam^{-1}.*

is resolved out by the (u, v) sampling. The much narrower absorption feature in the observed data suggests that the object may be viewed through a partially cleared cavity.

The effect of rotation on the single-dish line profiles toward the source center is small, either as a function of Ω or of inclination (Fig. 7.6). Inclination has its largest impact on the HCO^+ 4–3 line, which most exclusively samples dense material at small radii and with large velocities. Only for large values of Ω, where much of the inner region of the envelope has collapsed onto a disk, are the predicted single-dish lines much narrower than observed. This occurs because only the near-stationary outer regions of the envelope are left in the beam. Model results of Walker et al. (1994) and Zhou (1995) indicate that at larger distances from source center, where the infall velocities are smaller, solid-body rotation does have an observable impact on the shape of the line profiles.

7.4.2 Collapse of a magnetized cloud core

The centrifugal radius of $R_c \approx 800$ AU required to explain the observed flattening as due to rotation is uncomfortably large. As an alternative to rotation for the explanation of

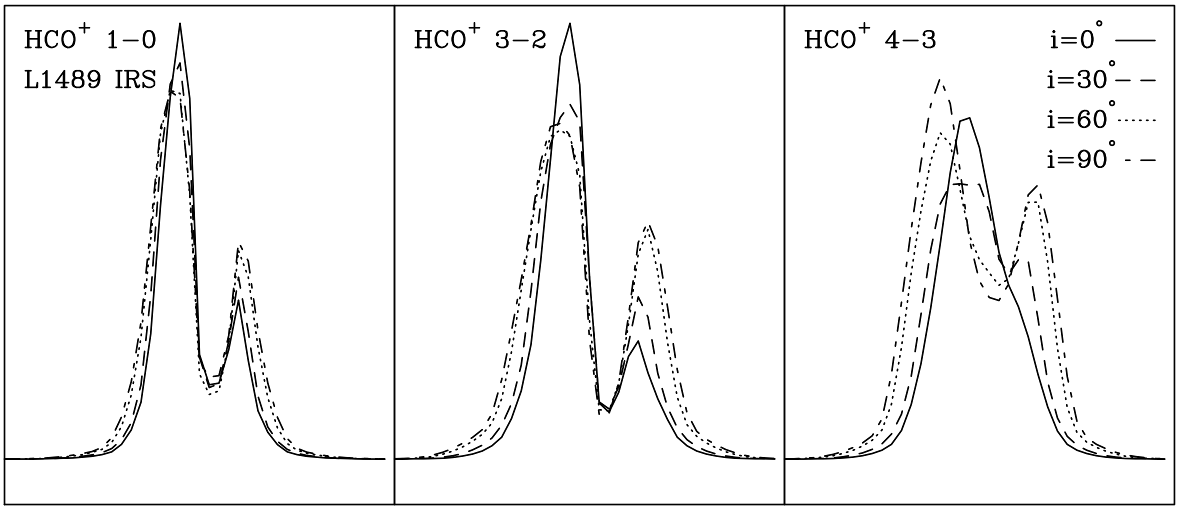

Fig. 7.6. *Model HCO^+ single-dish spectra for the slowly rotating, collapsing cloud. Different lines indicate inclinations of 0° (pole-on), 30°, 60°, and 90° (edge-on). Model parameters are those derived for L1489 IRS.*

a flattened structure, ordered magnetic fields are capable of partially supporting a cloud against self-gravity in one direction. Magnetic fields of 10–50 μG, which are thought to permeate interstellar clouds (e.g., Heiles et al. 1993; Crutcher et al. 1993), have been found to give rise to flattened structures, or pseudo-disks, in collapsing cores (Galli & Shu 1993a; Fiedler & Mouschovias 1993; Li & McKee 1996; Li & Shu 1997). Galli & Shu (1993a,b) model the influence of a weak magnetic field as a perturbation on the inside-out collapse model of Shu (1977), an approach which is valid for a dimensionless time $\tau < 1$, where $\tau = (B_0\sqrt{G}/2a)\ t$. The quantity $B_0\sqrt{G}/2a$ is the only combination of the magnetic field strength B_0, the gravitational constant G, and the sound speed a which has the dimension of s^{-1}. For intermediate values of the dimensionless spatial coordinate $x = r/at$, $0.2 < x < 1$, a semi-analytic solution for the density of the neutral species and velocity field is obtained, analogous to the formulation in monopole and quadrupole terms adopted by Terebey et al. ,

$$\rho_{\rm n}(r,\theta) = \frac{1}{4\pi G t^2}\ \Big[\alpha(x) + \tau^2\Big\{\alpha_{\rm M}(x) + \alpha_{\rm Q}(x)P_2(\cos\theta)\Big\}\Big], \tag{7.9}$$

$$V_r = a\ \Big[v(x) + \tau^2\Big\{v_{\rm M}(x) + v_{\rm Q}(x)P_2(\cos\theta)\Big\}\Big], \tag{7.10}$$

and

$$V_\theta = a\ \tau^2 w_{\rm Q}(x)\ \frac{d}{d\theta}P_2(\cos\theta), \tag{7.11}$$

where $\alpha(x)$ and $v(x)$ are the solutions for spherical collapse tabulated by Shu (1977), and the indices M and Q indicate the monopole and quadrupole terms tabulated by Galli & Shu (1993a). For $0.02 < x < 0.2$ numerical solutions for $\alpha(x,\theta)$, $V_r(x,\theta)$, and $V_\theta(x,\theta)$ are given by Galli & Shu (1993b).

The ions are fixed to the magnetic field lines, and so their distribution is different from that of the neutrals, with $\rho_{\rm i} \approx 3\times10^{-17}\sqrt{\rho_{\rm n}}$, where the numerical constant describes

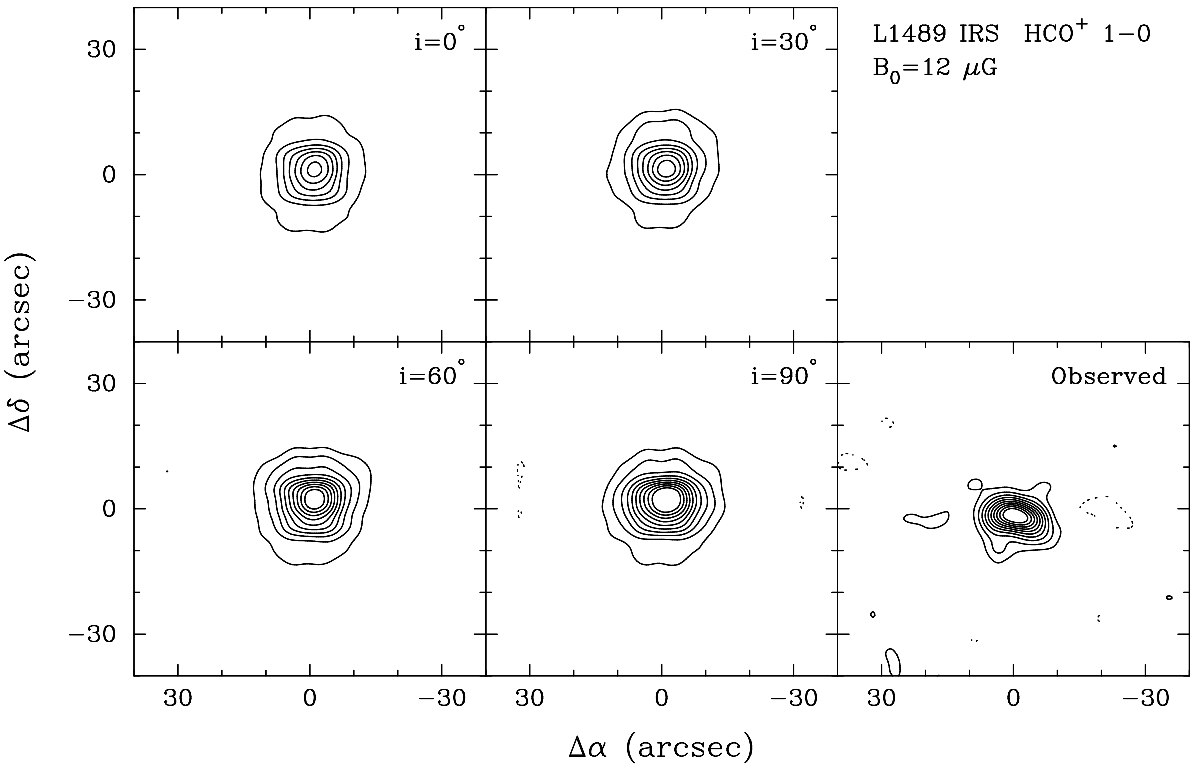

Fig. 7.7. *HCO^+ 1–0 images of a magnetized, collapsing core sampled at same (u, v) as OVRO data, and cleaned. Model calculations are for the derived parameters of L1489 IRS (Table 7.1), and include a magnetic field of 12 μG. The observed map is also shown; the position angle of the source equatorial plane is $\sim$65°. All maps are plotted at the same intensity levels of 0.06 Jy beam^{-1}.*

the coupling between neutrals and ions (Galli & Shu 1993b). When modeling the HCO^+ emission, we assume that HCO^+ follows the distribution of the neutrals for simplicity, in which case the HCO^+ abundance with respect to H_2 still applies.

Fig. 7.7 shows the resulting HCO^+ emission after sampling at the OVRO (u,v) points for L1489 IRS. A value of dimensionless time of $\tau = 0.7$ was adopted, corresponding to a field strength of $B_0 \approx 12$ μG for the age and sound speed derived in §7.3.2. Even when the source is viewed edge-on, $i = 90°$, the HCO^+ emission in the OVRO beam is only mildly flattened. This can be understood from the density distribution, compared in Fig. 7.3 to that of the model including rotation. Although the density distribution is highly flattened in the inner region, on a scale of $\sim$ 3000 AU or $\sim 20''$, the distribution is less flattened than in the case of rotation for $R_c = 800$ AU, especially after rotation of the distribution about the polar axis. For larger values of B_0, i.e., larger τ, a flatter density distribution will be obtained, but the perturbative method applied by Galli & Shu is no longer valid in this regime. The single-dish spectra are unaffected by the effects of flattening as predicted by the model.

An important distinction between magnetized and rotating collapsing cores lies in the azimuthal component of their velocity fields. As is seen in Fig. 7.8, the HCO^+ 1–0 position-velocity diagrams along the equator for different inclinations do not show

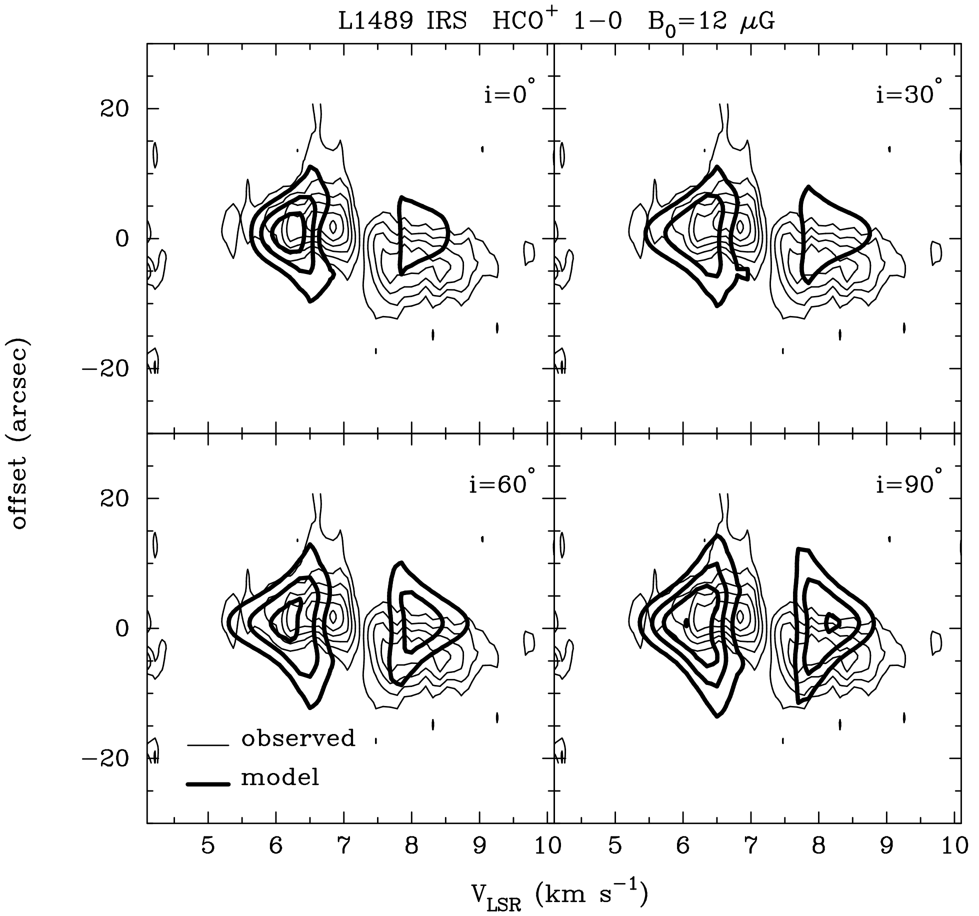

Fig. 7.8 *Overlay of observed position–velocity diagram of HCO^+ 1–0 in the OVRO beam toward L1489 IRS (thin lines), and model results for different inclinations and a magnetic field strength of 12 μG (heavy lines). For clarity, the model results are plotted at twice the contour intervals of the data, which is 0.35 Jy beam^{-1}.*

the red/blue asymmetry indicative of rotation seen in Fig. 7.5. The position-velocity diagram of L1489 IRS suggests that rotation is a better explanation for the observed structure than a magnetic field alone, although a combination of both is fairly probable.

Both models, that of Terebey et al. (1984) and Galli & Shu (1993a,b), are derived as a perturbation on the spherically symmetric model of Shu (1977). To explain the observed flattening, the parameters have to be stretched to the limits of the regime where this approach is valid. In hindsight this is not a surprising result: any process will only significantly influence the appearance of a model when it is no longer a small perturbation. The observations suggest that although a spherical model suffices on the size scale of single-dish observations, on the much smaller scales sampled by the interferometer, the envelopes deviate more from spherical symmetry than can be described by a simple perturbation. A full description of the effects of rotation and magnetic fields on the collapse of a cloud core is therefore warranted (cf. Li & Shu 1997).

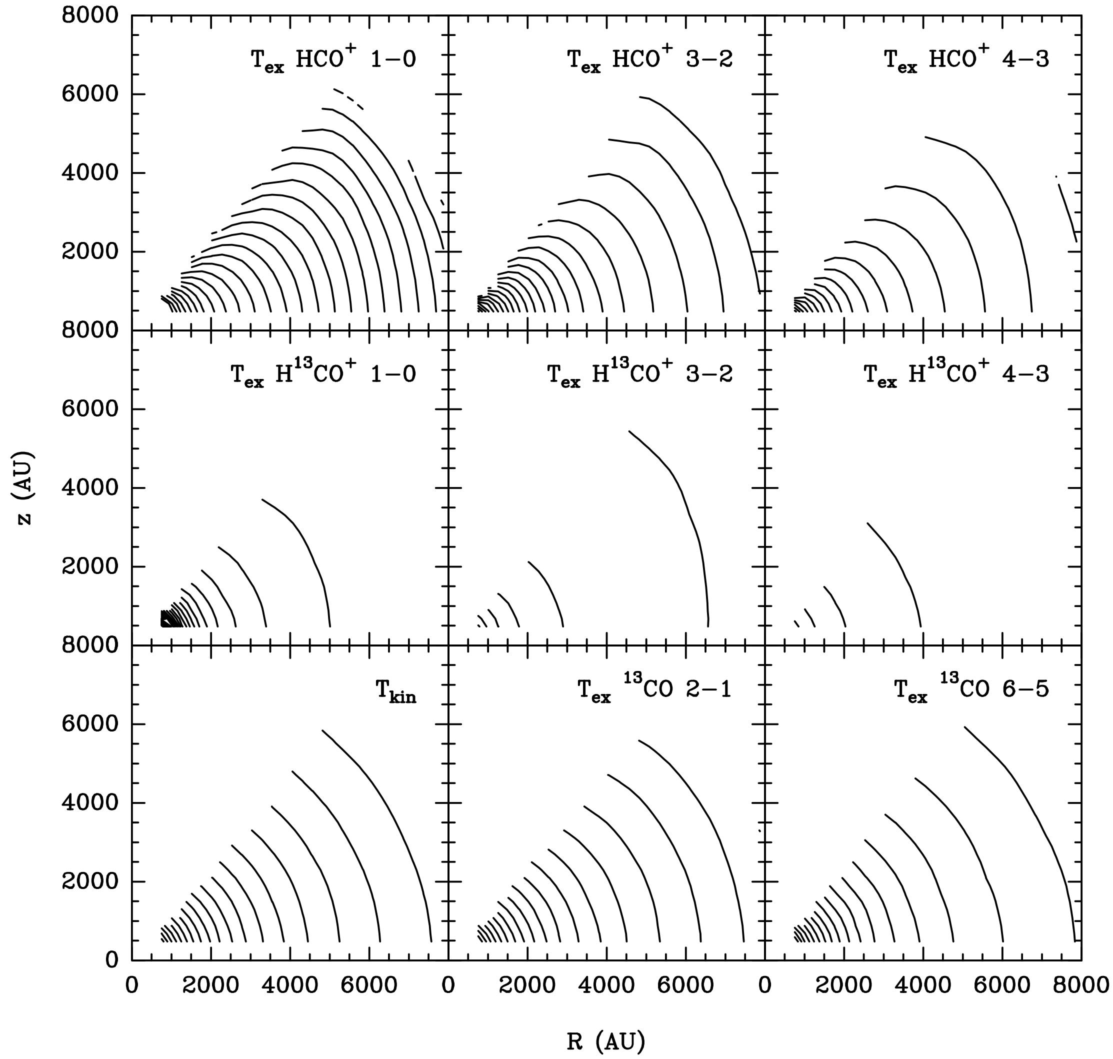

Fig. 7.9. *Excitation temperature of several lines in one quadrant of the source with a cavity evacuated by an outflow with half-opening angle of 40°. The kinetic temperature is depicted in the bottom left panel. The contours are drawn at 1 K intervals, starting at 13 K for $T_{\rm kin}$ and ^{13}CO 2–1, 8–9 K for ^{13}CO 6–5 and HCO$^+$ 1–0, and 4–6 K for the other panels.*

7.4.3 An evacuated outflow cavity

Even during the early, deeply embedded stage of their evolution, YSOs are found to drive bipolar outflows. Evacuated cavities can therefore be expected to be present in the surrounding envelopes from very early on in star formation. What is the influence of such cavities on the molecular excitation and the emergent line profiles? In this section we present model results for a spherical envelope, from which a cone with a half-opening angle of 40° has been cleared of material. This opening angle is suggested by the bright HCO$^+$ emission which appears to trace the cavity walls toward L1527 IRS (Chapter 3, Hogerheijde et al. 1998a, and below). The other model parameters a, t, and $X_{\rm mol}$ are assumed to be identical to those derived for L1527 IRS.

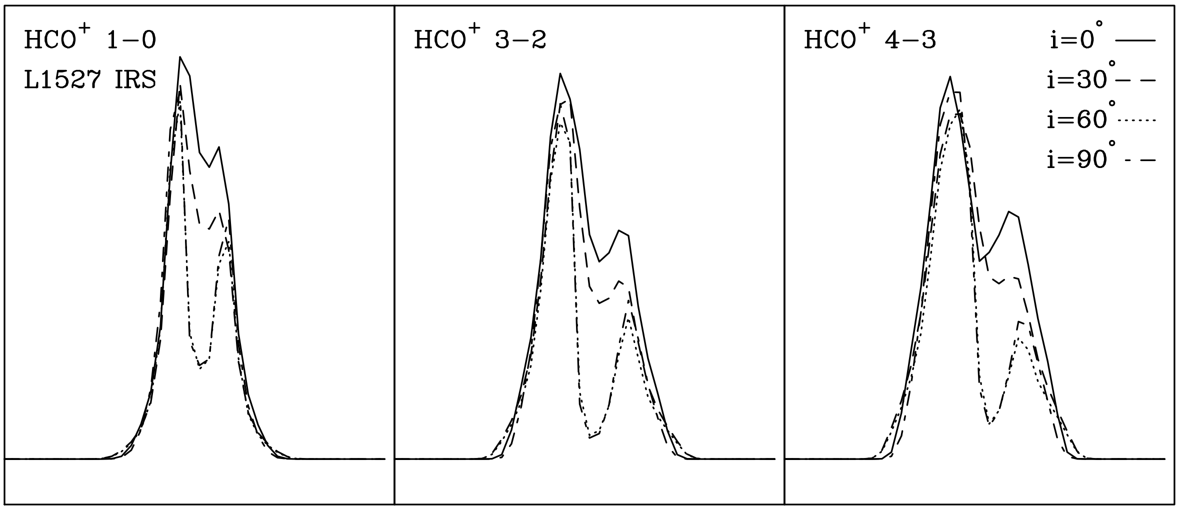

Fig. 7.10. *Model HCO^+ single-dish spectra with an evacuated outflow cavity. Different lines indicate inclinations of 0° (pole-on), 30°, 60°, and 90° (edge-on). Other model parameters are those derived for L1527. This source has an inclination of close to 90°.*

Figure 7.9 shows the excitation temperature of various transitions of HCO^+, $H^{13}CO^+$, and ^{13}CO, as well as the kinetic temperature in one quadrant of the source. The excitation of ^{13}CO closely follows the kinetic temperature since the densities are sufficient for thermalization throughout the envelope. The ^{13}CO 6–5 drops slightly below thermal levels only in the outer regions. Because the envelope is optically thin in this line, the presence or absence of an evacuated cavity is largely irrelevant. For this same reason, no effect is seen in the $H^{13}CO^+$ lines, even though the excitation is highly subthermal throughout the envelope. The only important effect of the cavity is on the excitation of HCO^+. The envelope has a significant optical depth in the plotted lines, and although the densities are too low for thermalization, the radiation field in the lines is strong enough to nearly thermalize the populations over a large region. This radiation field is especially strong at the center of the source, where the densities and temperatures are highest. The evacuated cavity provides a zero-opacity pathway for photons from the center to the material surrounding the cavity further out. This results in a layer of elevated excitation temperatures surrounding the cavity. The effect is limited to only a few percent, however, and no discernible effect is seen on the emergent brightness distribution of these lines.

The emergent profiles of the optically thick lines are, of course, affected by the presence of a cavity, even if there is little change in the excitation. The HCO^+ line profiles from envelopes with cavities are plotted in Fig. 7.10 for various inclinations. The depth of the self-absorption feature is especially sensitive to the source orientation. The orientation of L1527 IRS is close to edge-on, $i \approx 90°$ (cf. Chapter 3, Hogerheijde et al. 1998a).

Chapter 4 (Spaans et al. 1995) explores the effect of an evacuated outflow on the temperature structure of the surrounding envelope by allowing ultraviolet photons originating at the star–disk boundary layer to scatter into the molecular material. It was found that this process can contribute significantly to the temperature structure, giving rise to columns of 100 K gas comparable to those traced in ^{12}CO and ^{13}CO 6–5. Since this process is limited to regions for which the optical extinction does not exceed a few, it only operates efficiently in envelopes with comparatively low densities, like those surrounding TMR 1, L1489 IRS, and TMC 1. To what extent it dominates over the heating by infrared radiation remains to be determined. It is not a viable explanation for the bright HCO^+ and HCN emission lining the cavities toward L1527 IRS and SMM 1, since their excitation is not particularly sensitive to temperature.

7.5 A molecular mixing layer

This section investigates the bright HCO^+ and HCN emission outlining the outflow cavities of L1527 IRS and SMM 1 in terms of a mixing layer between the fast-moving outflow and the surrounding molecular envelope. Two characteristics of the emission lead us to propose such a model: (1) the emission occurs within a few km s^{-1} of the systemic velocity, and (2) it coincides with the intersection of the edges of the cavity with the plane of the sky, and is weak in between. A relatively thin conical layer of accelerated material reproduces these characteristics when viewed close to edge on, as is the case for L1527 IRS and SMM 1. Only tangential lines-of-sight sample material at projected velocities close to systemic, but still with sufficient radial velocity to shift the emission outside the line profile of the surrounding envelope. Radial lines-of-sight which cross the front and back of the cone sample material which is much more spread out in velocity and appears weak in emission.

7.5.1 A simple model

In the simple model constructed here, the mixing layer is assumed to extend over one-fifth of the total width of the outflow cavity, which has an opening angle of 45° as suggested by the HCO^+ and HCN images of L1527 IRS and SMM 1. The value for the width of the mixing layer is chosen somewhat arbitrarily, but it is found that a relatively thin layer is required to reproduce the observed contrast between tangential and radial lines-of-sight. The physical model discussed below is very simple, and serves only to illustrate how a mixing layer can explain the HCO^+ and HCN observations.

Theoretical models of the outflows driven by low-mass YSOs and their interaction with the surrounding envelopes are given by, e.g., Shu et al. (1995) and Li & Shu (1996a). A recent overview of the astrophysical aspects of mixing layers between two moving fluids can be found in Raga & Cantó (1997). The density, temperature, and velocity fields in a mixing layer will depend in detail on hydrodynamic processes, and are likely to involve turbulence (cf. Rawlings & Hartquist 1997). Here, we will construct a simple model for the average density and temperature as functions of position in the flow, based on the so-called Couette flow solution (cf. also Giovanardi et al. 1992, and Stahler 1994). In laboratory experiments quoted by Raga & Cantó (1997) the mean flow velocity in a mixing layer between a moving and a stationary fluid is found to depend linearly on the distance from the layer's edge (Couette flow). The flow velocity $V(\ell)$ is then given by

$$V(\ell) = V_{\rm flow}(\ell/L), \tag{7.12}$$

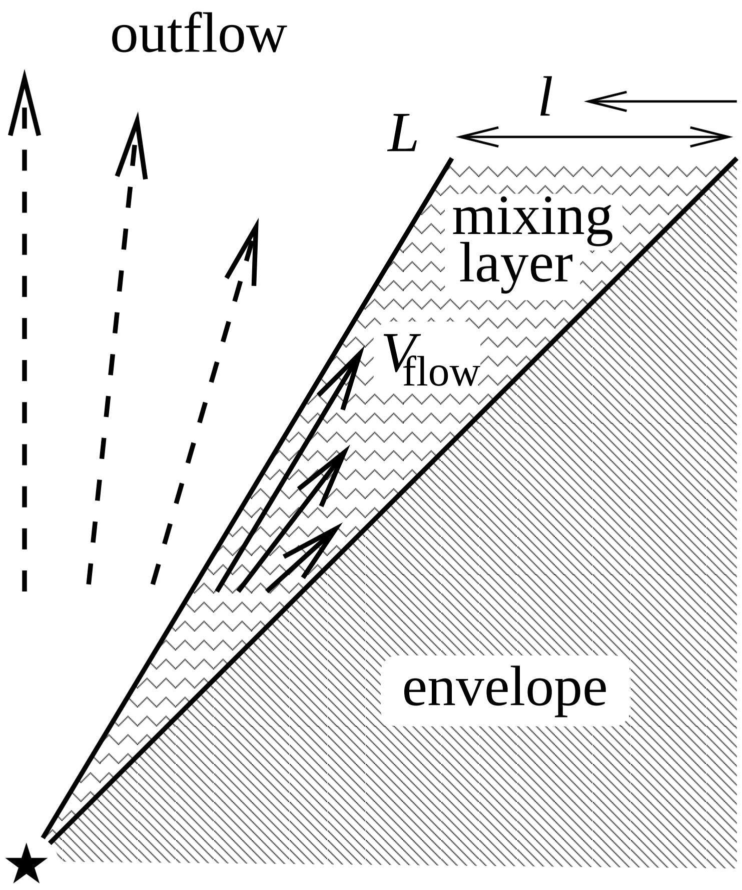

Fig. 7.11. *Sketch of the adopted model for the mixing layer between the outflow and the surrounding envelope.*

where ℓ is the distance measured from the edge of the envelope, and L the width of the mixing layer of one-fifth of the cavity. $V_{\rm flow}$ is the velocity along the inner edge (see Fig. 7.11). We further assume that the velocities are directed radially from the star. On top of the smooth flow there will be turbulent motions, with $\Delta V \ll V(\ell)$. A value of $\Delta V = 0.2$ km s^{-1} is adopted. The excitation and radiative transfer of the material in the flow will be dominated by the gradient in the systemic velocity field.

Stahler (1994) quotes the observational result for molecular outflows that the mass decreases with velocity as $dm(V)/dV \propto V^{-\gamma}$, with $\gamma \approx 1.9$. If the density n does not depend explicitly on V, $n(\ell)$ follows from $dm(V)/dV$ and equation (7.12),

$$n(\ell) = n_0 \left(1 - \frac{\ell}{L}\right)^{\gamma} \quad (\gamma \approx 1.9), \tag{7.13}$$

where the density smoothly joins the surrounding envelope at $\ell = 0$ with $n = n_0$. Because of the arbitrary choice for the width of the mixing layer of one-fifth of the total width of the outflow cavity, a fudge factor η is required to fix the total amount of material in the mixing layer. The value of η is adjusted to reproduce the level of emission in the ^{12}CO line wings.

The temperature distribution in the mixing layer is obtained under the assumption of pressure equilibrium, $nT_{\rm kin}$ = constant, so that $T_{\rm kin}(\ell) = T_{\rm kin}(0)\ [1 - \ell/L]^{-\gamma}$. Formally

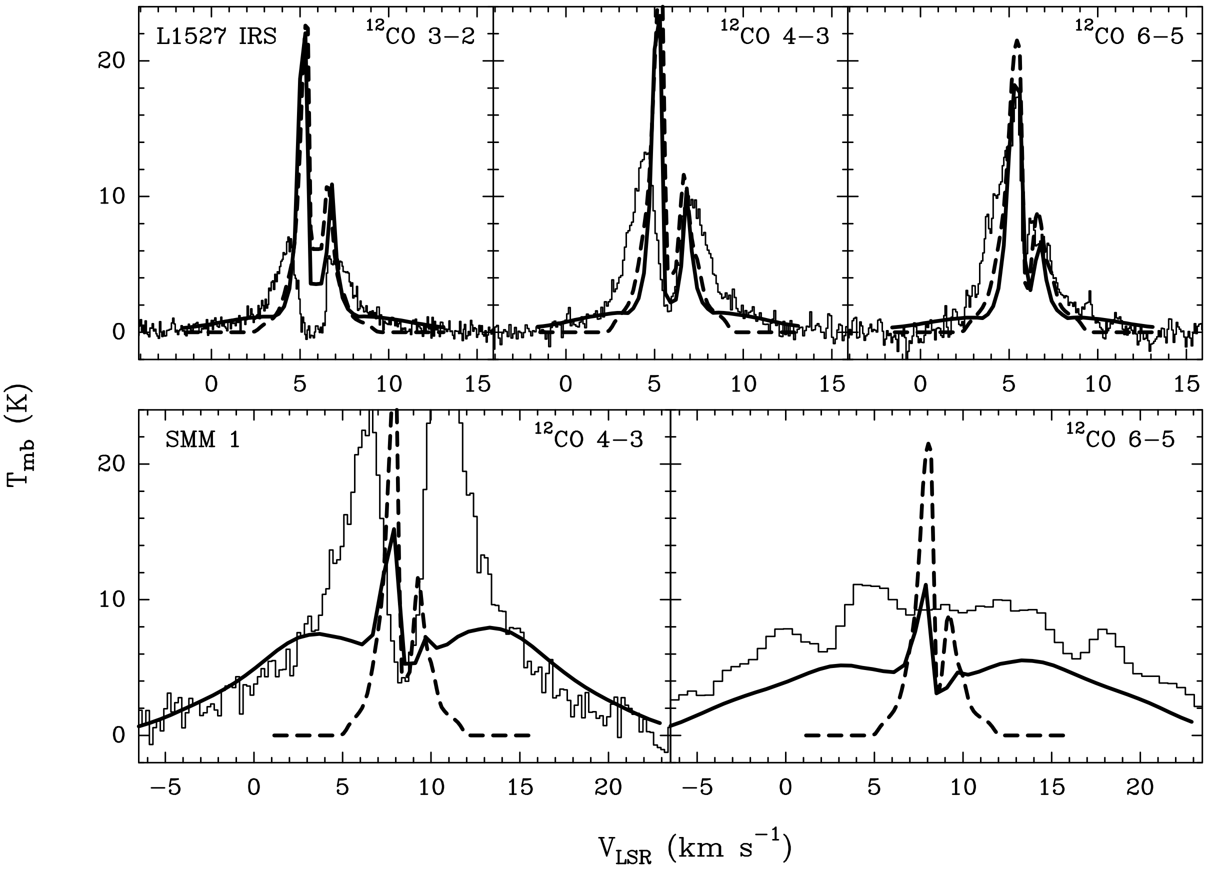

Fig. 7.12. *Observed ^{12}CO spectra toward L1527 IRS (top) and SMM 1 (bottom), overlaid with best-fit spherically symmetric envelope models (dashed line) and best-fit models of envelope and mixing layer as described in §7.5 (solid line).*

this expression diverges as $\ell \to L$, but this does not influence the emission since the density approaches zero in that limit.

Collisions with electrons can contribute significantly to the excitation of species with large dipole moments such as HCO^+ and HCN. In the molecular envelope the electron fraction with respect to H_2 is assumed to be low, $X_e < 10^{-6}$, consistent with dark cloud chemistry. However, the outflow is likely to be partially ionized, and the electron fraction in the mixing layer may exceed $\sim 10^{-5}$, where their contribution to the excitation of HCO^+ and HCN becomes significant. For the excitation of CO electron collisions are unimportant at the densities considered here because it has a much smaller dipole moment of 0.1 Debye, as compared to 3.9 and 3.0 Debye for HCO^+ and HCN, respectively (Millar et al. 1991). In the modeling of the HCO^+ and HCN emission, X_e is a free parameter.

Additional free parameters for the HCO^+ and HCN models are their respective abundances. From a highly idealized mixing layer model, Taylor & Raga (1995) find that the HCO^+ abundance with respect to H_2 may be enhanced by up to two orders of magnitude to 10^{-7}, through the reaction $CH + O \to HCO^+ + e^-$.

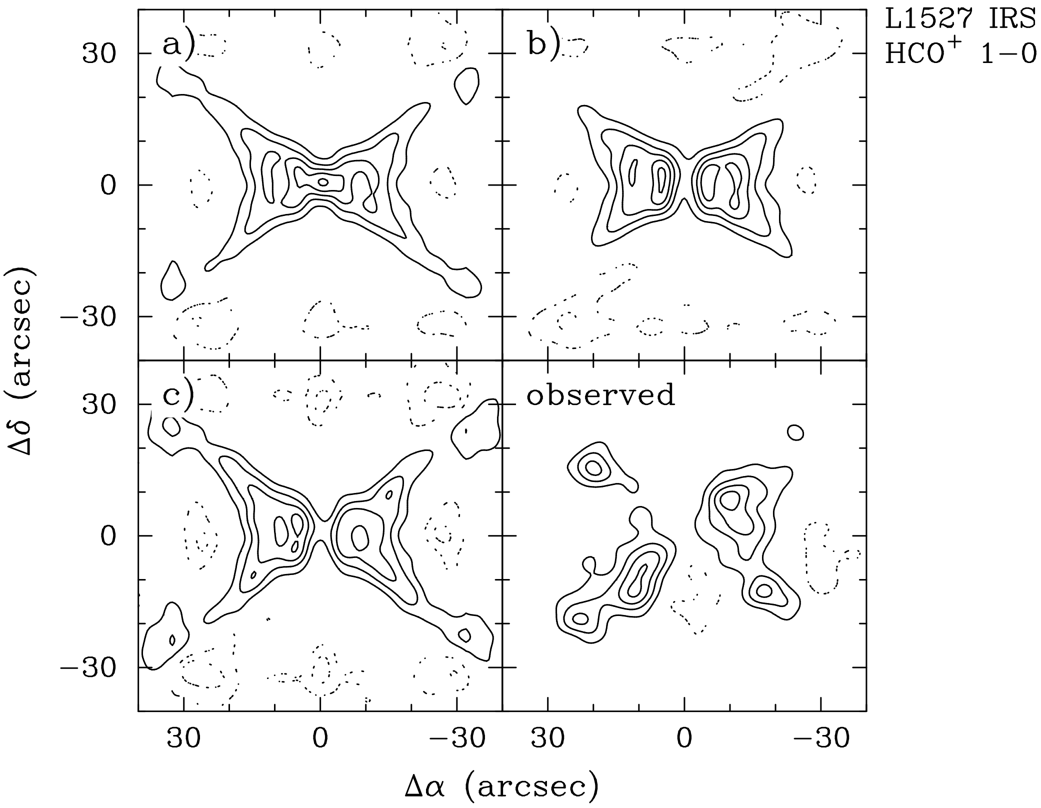

Fig. 7.13. *Comparison of the results of the mixing layer model with the observed HCO^+ emission toward L1527 IRS (lower left panel). The model results have been sample at the (u,v) positions of the data, which are plotted with contour levels of 0.06 Jy beam^{-1}.* **(a)** $X(\mathrm{HCO}^+) = 8\times10^{-9}$ *as in the envelope, and X_e =0, plotted at 1/30 of the intensity level of the data.* **(b)** *HCO^+ abundance increased by a factor of 20, and $X_e = 0$, plotted at twice the intensity level of the data.* **(c)** $X(\mathrm{HCO}^+) = 8 \times 10^{-9}$ *as in the envelope, and $X_e = 10^{-4}$, plotted at 1/3 of the intensity level of the data.*

7.5.2 Results

Values for the model parameter $V_{\rm flow}$ and η are derived from approximate fits to the ^{12}CO 3–2, 4–3, and 6–5 line wings of L1527 IRS and SMM 1. Since only radial velocities are reflected in the spectra, the derived $V_{\rm flow}$ values depend on the adopted opening angle of 45° and source inclination $i = 90°$. L1527 IRS is viewed almost edge-on ($i = 90°$). The inclination of SMM 1 is less well constrained, but $i \approx 90°$ is probably a good estimate. For L1527 IRS we find $V_{\rm flow} = 20$ km s^{-1} and $\eta = 0.5$. The much more prominent outflow wings toward SMM 1 yield $V_{\rm flow} = 30$ km s^{-1} and $\eta = 0.8$. The resulting model spectra are shown in Fig. 7.12. Although these fits are only approximate, they provide useful constraints on the velocities and the amount of material in the mixing layers.

Figures 7.13 and 7.14 show the resulting HCO^+ and HCN images after convolving at the (u, v) positions of the OVRO data for the derived values of $V_{\rm flow}$ and η. The central 2–3 km s^{-1} where the envelope dominates the emission have been removed from the model, corresponding to the resolved-out large-scale emission in the data. Three

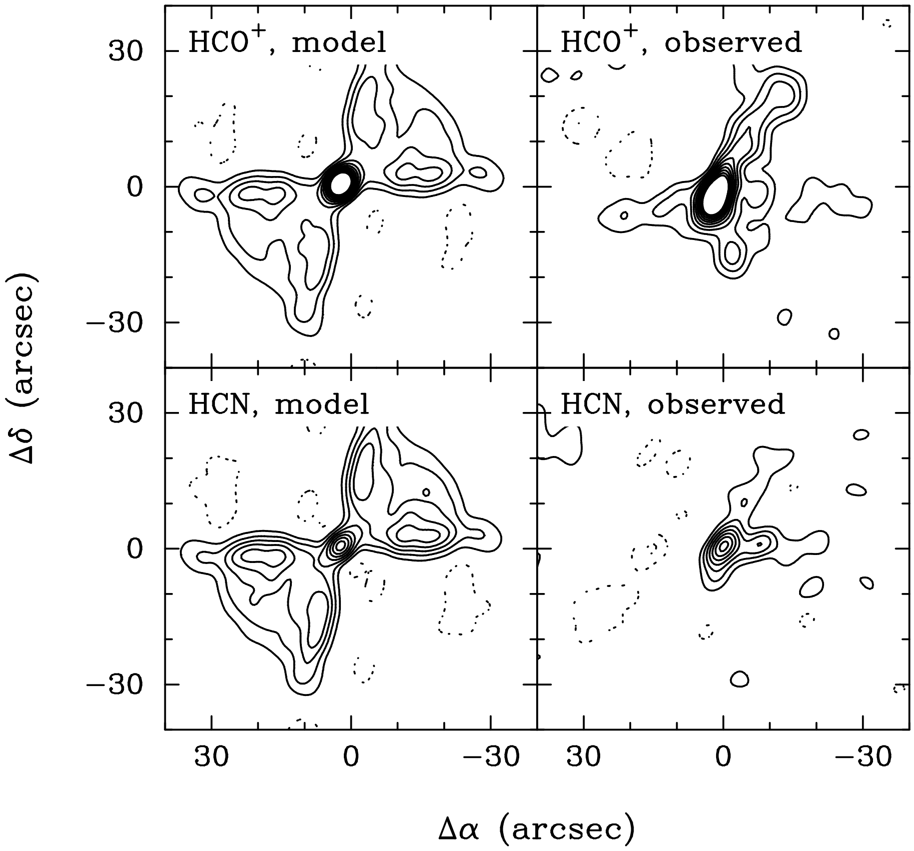

Fig. 7.14. *Comparison of the results of the mixing layer model with the observed HCO$^+$ (top panels) and HCN (lower panels) emission toward SMM 1. The model results (left panels) have been sample at the (u,v) positions of the data (right panels), which are plotted with contour levels of 0.04 Jy beam^{-1} and 0.05 Jy beam^{-1}, respectively. The models have HCO$^+$ and HCN abundances of 6×10^{-9} and 3×10^{-8}, respectively, similar to those inferred for the envelope. For the densities involved here, collisions with electrons do not contribute significantly to the excitation. The models are plotted at 1/4 of the intensity of the HCO$^+$ observations and at 1/2 of the HCN observations.*

different models are calculated for L1527 IRS (Fig. 7.13). The first model has an HCO$^+$ abundance equal to that found in the envelope, $X(\mathrm{HCO}^+) = 8 \times 10^{-9}$, and an electron fraction $X_e = 0$. Although the shape of the emission corresponds well with the observed HCO$^+$ emission, the absolute intensity is too low by a factor of ~ 30. The second model has the HCO$^+$ abundance increased by a factor of 20, producing an intensity level comparable to the observations. The increased opacity, however, completely fills the cone with emission. The third model circumvents this problem by using the original HCO$^+$ abundance of 8×10^{-9} and an electron fraction of 10^{-4}. This increases the excitation, and gives better correspondence to the observations. Although quantitative conclusions cannot be drawn from our simplified model, the results indicate that the bright HCO$^+$ outlining the cavity of L1527 IRS can be explained by a mixing layer with at most a mildly enhanced HCO$^+$ abundance and an electron fraction of $\sim 10^{-4}$.

For SMM 1 only one set of models is calculated (Fig. 7.14). The much larger densities in its envelope, which determine the density structure in the mixing layer (eq. 7.13), ensure that the HCO^+ excitation is sufficient to produce emission at the observed intensity. Electrons contribute negligibly to the excitation compared to H_2 at these densities. To reproduce the spatial extent of the HCO^+ and HCN emission, the radius of the envelope around SMM 1 has been extended to 16000 AU, corresponding to the more extended cloud around this source. Although the HCO^+ and HCN intensity in the resulting images is largest along the edges of the cavity, the contrast with the interior of the cone does not match the observations. Most likely our simple model misses some of the details of the width of the mixing layer and its velocity structure.

The results presented in this section show that a simple model for a mixing layer between a molecular envelope and a atomic or partially ionized outflow or wind can explain the observed ^{12}CO line wings and the bright emission of HCO^+ and HCN which outlines the outflow in interferometer observations. Such mixing layers contribute no more than a few percent to the HCO^+ and HCN emission observed in single-dish beams. The presented model is highly simplified, and more physical and chemical processes need to be included before detailed quantitative conclusions can be reached, but it is clear that millimeter interferometry of species like HCO^+ and HCN provides a promising tool to spatially resolve these mixing layers and to directly probe their physics and chemistry.

7.6 Conclusions

The Monte Carlo methods developed in this chapter form a necessary and valuable step in the interpretation of the molecular line observations in terms of models of protostellar collapse. The involved computation time allows a full parameter space study of spherically symmetric, or one-dimensional, models. These then serve as starting points for more detailed axisymmetric or two-dimensional model calculations, which require significantly more time. The results obtained with this combined approach can be summarized as follows.

1. The spherically symmetric inside-out collapse model formulated by Shu (1977) reproduces well many of the single-dish and interferometer molecular lines, with the exception of obvious cases like outflow wings, small-scale structure associated with rotation, outflows, or absorption by cold foreground material. This indicates that over scales between 1000 and 10,000 AU, the density, temperature, and velocity structure of this spherically symmetric model is an accurate description of the envelopes.

2. The model parameters sound speed a and age t are accurately constrained by the line intensities and profile shapes. The inferred values are listed in Table 7.1 together with estimates of the HCO^+ and HCN abundances. The corresponding envelope masses within $\sim 20''$ diameter regions correspond well with estimated dust masses. For the obtained values of a and t, the model predicts accretion luminosities exceeding the observed bolometric luminosity by factors of 5–35. This discrepancy has been noted before, and suggests that most material accretes onto a circumstellar disk before flowing onto the star at a much lower, or time-varying, rate.

3. To derive accurate estimates of the molecular abundance from interferometer observations, the missing zero-spacing flux has to be taken into account explicitly. One

way of doing that is by sampling results of model calculations at the same (u,v) positions as the data. With this method, no large abundance variations in HCO^+ or HCN are found between the scales sampled by the interferometer and single-dish observations. Differences by factors of a few between the modeled and observed interferometer line intensities can easily be due to deviations from the adopted density, temperature, and velocity structure.

4. The observed flattening and some of the characteristics of the velocity structure on a scale of $\sim$ 1000 AU toward, e.g, L1489 IRS, can be reproduced by including rotation in the collapse solution, as formulated by Cassen & Moosman (1981) and Terebey et al. (1984). To match the observations, a centrifugal radius of order R_c = 400–800 AU seems to be required. This is uncomfortably large, since the model assumes that all material is collapsed onto a disk within this radius. A smooth description of the transition of a collapsing envelope to a circumstellar disk is needed to further investigate these regions.

5. A similar degree of flattening on a scale of $\sim$ 1000 AU is produced by a weak, ordered magnetic field, as modeled by Galli & Shu (1993a). The observed rotation signature in the position-velocity diagram is not reproduced, of course. A combination of rotation and a magnetic field also forms a likely model for the observations (e.g., Li & Shu 1996b).

6. A simple model for the mixing layer set up between the outflow and the molecular envelope is capable of qualitatively explaining the bright HCO^+ and HCN emission which outlines the cavity in the interferometer beam, together with the ^{12}CO outflow wings. To reproduce the observed emission peak at the intersection of the conical mixing layer with the plane of the sky, the mixing layer has to extend over no more than one-fifth of the full width of the cavity. With an electron fraction of $\sim 10^{-4}$ the excitation of HCO^+ and HCN is sufficient to generate the observed intensity levels without any abundance enhancements of these species. Observation of the 3–2 lines is required to better constrain the excitation, and to put firmer limits on the electron fraction and abundances of HCO^+ and HCN.

This chapter illustrates the crucial role of detailed model calculations in the interpretation of molecular line data, especially interferometric images which suffer from large levels of resolved-out, extended flux. With a well chosen data set of single-dish lines of CO, HCO^+, and HCN, and their isotopomers, the envelope structure of a large sample of YSOs can be investigated within the frame work of the spherically symmetric inside-out collapse model. The proposed mixing layer model offers a promising observational tool to probe the dynamical and chemical interaction of outflowing material with molecular cores.

Acknowledgments M. Spaans is thanked for discussions which led to the formulation of our Monte Carlo code, during which time the Johns Hopkins University provided hospitality. L. Mundy contributed to the original version of the radiative transfer code used in this work. M. R. H. is indebted to the Netherlands Organization for Scientific Research (NWO) and the Leids Kerkhoven-Bosscha Fonds for travel support. Research in Astrochemistry in Leiden is supported by NWO/NFRA through grant no. 781–76–015.